AFRL-AFOSR-VA-TR-2022-0355

Dynamically Reconfigurable, Conformal, Metasurface Apertures for Communications and Sensing Applications in Aerospace Platforms

SMITH, DAVID
DUKE UNIVERSITY
2200 W MAIN ST STE 710
DURHAM, NC, 27708
USA

07/07/2022
Final Technical Report

Air Force Research Laboratory
Air Force Office of Scientific Research
Arlington, Virginia 22203
Air Force Materiel Command

REPORT DOCUMENTATION PAGE

PLEASE DO NOT RETURN YOUR FORM TO THE ABOVE ORGANIZATION.

1. REPORT DATE	2. REPORT TYPE	3. DATES COVERED	
20220707	Final	START DATE 20180915	END DATE 20211231

4. TITLE AND SUBTITLE
Dynamically Reconfigurable, Conformal, Metasurface Apertures for Communications and Sensing Applications in Aerospace Platforms

5a. CONTRACT NUMBER	5b. GRANT NUMBER	5c. PROGRAM ELEMENT NUMBER
	FA9550-18-1-0526	61102F
5d. PROJECT NUMBER	**5e. TASK NUMBER**	**5f. WORK UNIT NUMBER**

6. AUTHOR(S)
DAVID SMITH

7. PERFORMING ORGANIZATION NAME(S) AND ADDRESS(ES)
DUKE UNIVERSITY
2200 W MAIN ST STE 710
DURHAM, NC 27708
USA

8. PERFORMING ORGANIZATION REPORT NUMBER

9. SPONSORING/MONITORING AGENCY NAME(S) AND ADDRESS(ES)	10. SPONSOR/MONITOR'S ACRONYM(S)	11. SPONSOR/MONITOR'S REPORT NUMBER(S)
Air Force Office of Scientific Research 875 N. Randolph St. Room 3112 Arlington, VA 22203	AFRL/AFOSR RTB1	AFRL-AFOSR-VA-TR-2022-0355

12. DISTRIBUTION/AVAILABILITY STATEMENT
A Distribution Unlimited: PB Public Release

13. SUPPLEMENTARY NOTES

14. ABSTRACT
The goal of this program was to investigate the use of waveguide-fed metasurface antennas in the context of conformal array antennas. During this report period, the team has completed the major tasks of developing the design and calibration frameworks, arriving at a passive prototype conformal antenna array that made use of the developed tools and demonstrated the key concepts. One key result is the completion of the coupled-dipole formalism modified for arbitrary conformal metasurface antenna geometries. This fast, quasi-analytical modeling tool enables the prediction not only of the directivity and field patterns associated with a given metasurface antenna design, but also of the efficiency, gain, reflection and other system parameters necessary to fully assess the potential performance of a conformal metasurface array antenna. As a complement to the dipole modeling, a quasi-analytical perturbative method has been developed to predict the guided mode associated with an arbitrarily curved waveguide. Given that the dipole modeling tool requires accurately computed waveguide fields, the perturbative provides an important component of the completed framework. Using the perturbative approach, it can be seen that for mild curvature the unperturbed waveguide modes are a reasonable approximation, simplifying the overall design for most cases. For situations where extreme curvature might be necessary—as at certain points on aircraft wings or nose cones—the modeling tool can now be applied to obtain accurate predictions. In a final experimental study, a passive metasurface conformal array was designed, fabricated and tested. The antenna was fabricated using a multilayer printed circuit board (PCB) technique, with the waveguide layer formed in a substrate integrated waveguide (SIW) layer. In addition to the array of metasurface antennas, a conformal, corporate feed structure was designed and integrated with the PCB antenna. In parallel, the team continued progress in developing the orthogonal coded near-field (OCNF) calibration technique. In this novel calibration approach, every element of the metasurface array can be comprehensively characterized with a minimum of scans and acquired data sets, resulting in a rapid and efficient calibration process that can be applied not only to conformal metasurface arrays, but many other array antenna systems. The approach was validated with numerical simulations that emulate the experimental configurations, with initial measurements performed on metasurface test coupons. In summary, the metasurface antenna represents a new platform that is ideally suited to conformal array antennas, addressing the most challenging issues associated with these systems. In particular, the reduced complexity of the metasurface antenna—a result of the absence of complicated transmit/receive modules containing phase shifters, amplifiers and other devices—allows a lower profile structure that can be readily bent and integrated into curved structures. The initial steps taken in this two-year program form a roadmap for future implementations and transition of this important technology.

15. SUBJECT TERMS

16. SECURITY CLASSIFICATION OF:			17. LIMITATION OF ABSTRACT	18. NUMBER OF PAGES
a. REPORT	b. ABSTRACT	c. THIS PAGE		
U	U	U	UU	50

19a. NAME OF RESPONSIBLE PERSON	**19b. PHONE NUMBER** *(Include area code)*
ARJE NACHMAN	426-8427

Final Technical Report:

Dynamically Reconfigurable, Conformal Metasurface Apertures for Communications and Sensing Applications in Aerospace Platforms

Defense Enterprise Science Initiative (FA9550-18-1-0526)

Reporting Period: 15 Sep 2019 through 31 Dec 2020
Program Period: 15 Sep 2018 through 31 Dec 2020

PI: David Smith, Duke University
co-PI: Matthew Reynolds, University of Washington
co-PI: Vesna Radisic, Northrop Grumman

Executive Summary

The goal of this program was to investigate the use of waveguide-fed metasurface antennas in the context of *conformal array antennas*. During this report period, the team has completed the major tasks of developing the design and calibration frameworks, arriving at a passive prototype conformal antenna array that made use of the developed tools and demonstrated the key concepts. One key result is the completion of the coupled-dipole formalism modified for arbitrary conformal metasurface antenna geometries. This fast, quasi-analytical modeling tool enables the prediction not only of the directivity and field patterns associated with a given metasurface antenna design, but also of the efficiency, gain, reflection and other system parameters necessary to fully assess the potential performance of a conformal metasurface array antenna. As a complement to the dipole modeling, a quasi-analytical perturbative method has been developed to predict the guided mode associated with an arbitrarily curved waveguide. Given that the dipole modeling tool requires accurately computed waveguide fields, the perturbative provides an important component of the completed framework. Using the perturbative approach, it can be seen that for mild curvature the unperturbed waveguide modes are a reasonable approximation, simplifying the overall design for most cases. For situations where extreme curvature might be necessary—as at certain points on aircraft wings or nose cones—the modeling tool can now be applied to obtain accurate predictions. In a final experimental study, a passive metasurface conformal array was designed, fabricated and tested. The antenna was fabricated using a multilayer printed circuit board (PCB) technique, with the waveguide layer formed in a substrate integrated waveguide (SIW) layer. In addition to the array of metasurface antennas, a conformal, corporate feed structure was designed and integrated with the PCB antenna. In parallel, the team continued progress in developing the orthogonal coded near-field (OCNF) calibration technique. In this novel calibration approach, every element of the metasurface array can be comprehensively characterized with a minimum of scans and acquired data sets, resulting in a rapid and efficient calibration process that can be applied not only to conformal metasurface arrays, but many other array antenna systems. The approach was validated with numerical simulations that emulate the experimental configurations, with initial measurements performed on metasurface test coupons. In summary, the metasurface antenna represents a new platform that is ideally suited to conformal array antennas, addressing the most challenging issues associated with these systems. In particular, the reduced complexity of the metasurface antenna—a result of the absence of complicated transmit/receive modules containing phase shifters, amplifiers and other devices—allows a lower profile structure that can be readily bent and integrated into curved structures. The initial steps taken in this two-year program form a roadmap for future implementations and transition of this important technology.

Program Tasks:

The following list of tasks appeared in the proposal and are partially updated in this annual report.

THRUST (I): CONFORMAL ANTENNA DESIGN

Task I.1: *Conformal Metasurface Antenna Design*

Completed in the previous report period. The SIW-PCB based metasurface antenna design was selected as the basis for the array antenna.

THRUST (II): ANALYTICAL AND NUMERICAL MODELING

Task II.1: *Analyze the Dispersion and Electromagnetic Modes of a Conformal Waveguide*

Two techniques were developed. The first, based on conformal mapping, was completed in the previous report period. The second, a more general approach valid for arbitrarily curved waveguides, was completed in this report period in terms of implementation and final illustrative calculations.

Task II.2: *Modeling of Tunable Metamaterial Resonators for Conformal SIW and CPW Architectures*

Two techniques were developed. The first, based on conformal mapping, was completed in the previous report period. The second, a more general approach valid for arbitrarily curved waveguides, was completed in this report period in terms of implementation and final

Task II.3.1: *Analysis of Conformal Metasurface Antennas*

This report period, the complete coupled-dipole framework for conformal antennas was implemented, allowing accurate and complete modeling of conformal metasurface array antenna designs. The approach was used to design the experimental sample eventually produced and tested.

Task II.3.2: *Synthesis of Patterns from Conformal Metasurface Antennas*

This report period, an optimization approach was applied in conjunction with the coupled-dipole modeling to arrive at the metamaterial element designs across the conformal metasurface antenna. The completion of Task II.3.1 enabled the iterative optimization approach to be applied in this task.

Task II.4: *Design of Feed Structure*

In this report period, a corporate feed structure compatible with the conformal metasurface array antenna was designed using quasi-analytical techniques that could be incorporated with the coupled-dipole formalism. The designed feed structure was also fabricated and used in the final experimental sample.

THRUST (III): ANTENNA CALIBRATION, OPTIMIZATION AND ORTHOGONALLY CODED NEAR FIELD (OCNF) SCAN DEVELOPMENT

Task III.1: *Metasurface Control Plane design and fabrication*

The development of a dynamically reconfigurable, conformal metasurface array antenna was not accomplished during this program, as a result of other program priorities combined with lab restrictions and delays due to COVID. Given the accomplishments achieved in this

program, we feel the control layer can be easily adapted from the planar structures to the conformal structures and suggest this as near-term future work for potential follow-on efforts. During this reporting period, a single element test coupon (planar sample) was measured and analyzed, allowing some key aspects of the OCNF method to be evaluated.

Task III.2: *Digital Control Logic and OCNF Modulation design and fabrication*

During this report period, a variety of OCNF modulation schemes were considered and evaluated in Monte Carlo simulations. An optimal modulation scheme was identified and validated through this process. Implementation to digital control logic was not pursued, given other program priorities and the lab restrictions due to COVID.

Task III.3: *OCNF Demodulation and Integration with Conventional Near-Field Scan Data*

During this report period, the OCNF demodulation was performed using near-field scan data acquired from a single element test coupon. The goal of this preliminary experiment was to extract the effective polarizability of the element as a function of frequency and possibly other state variables (such as temperature, mask pattern, etc.). During the experiments, it was found that the feed section of the assembly was also radiating, producing a signal that interfered with that of the single element. Given the lab restrictions and an inability to produce and measure additional samples, a preliminary model was developed to account for the unwanted leakage. Applying this model to remove the leakage signal, a characterization of the polarizability was performed using the near-field scanned data, validating the OCNF method. The unwanted leakage can be removed in future samples and measurements.

THRUST (IV): PROOF-OF-CONCEPT DEMONSTRATION

Task IV.1: *Sample Fabrication and Experimental Verification*

During this report period, a sequence of test conformal metasurface antenna samples were produced and measured. Initially, a simple 1D conformal metasurface antenna was designed, simulated and measured. The antenna was designed to produce a collimated beam in the broadside direction. The resulting beam showed excellent agreement with simulations. Further indicating the design specificity, when the antenna was flattened the collimated beam disappeared, as expected. Subsequently, several complete conformal metasurface array antennas were produced using a commercial printed circuit board (PCB) vendor. These static (not dynamically reconfigurable) antennas consisted of an array of 1D metasurface waveguide-fed antennas, excited using a co-designed corporate feed structure also fabricated in the PCB stackup. Several antennas were produced, designed to generate beams in several different directions. The antennas were designed using the dipole framework, validated with numerical simulations, and ultimately measured experimentally. Excellent agreement was found between theory and experiment, providing the ultimate validation of the techniques developed in this program.

Technical Narrative

The goal of this program was to investigate the use of waveguide-fed metasurface antennas in the context of *dynamically reconfigurable conformal array antennas*. Conformal antennas—antennas that conform to a surface whose shape is determined by considerations other than electromagnetic [1]—are crucial for modern military and commercial vehicles. The required apertures for the large and growing number of communications and radar antenna systems can produce drag, degrading overall performance of the asset, as well as increasing backscatter, making the asset more detectable and thus easier to target. For large commercial aircraft there are at least 20-30 antennas that protrude from the aircraft skin [2], and oftentimes many more than that. Since it is desirable to electronically steer most antennas, the necessary bias and control circuitry that reconfigures the aperture must also be integrated into the low-profile structure, adding a significant extra burden for conformal antennas.

Aside from the evident advantage of reduced drag, reconfigurable conformal antenna arrays have many additional benefits over planar arrays, including directivity/gain that does not necessarily drop off with scan angle; very large angular coverage; reduced radar cross section; and no conventional radome needed. However, conformal array antennas are still not implemented widely due to several issues that our program was designed to address. We summarize those issues here.

Design and Modeling: The design of conformal array antennas has typically involved a combination of analytical and quasi-analytical methods that are not easily adapted for arbitrarily curved surfaces. A small number of geometries comprising ideal dipoles yield closed-form equations [3]—such as a cylindrical array—but these solutions do not form the basis of a complete design tool. While full-wave simulations can provide exact solutions to arbitrary geometries and materials, the lack of symmetry associated with singly and doubly curved arrays means that the entire structure must be simulated. The computational domain for even moderate sized arrays can be extremely large, resulting in long run times and immense storage requirements. Such simulations are not feasible, especially given the many iterations needed for design and optimization.

Reconfigurable Architecture: To achieve reconfigurability, each of the radiating elements in an array must be addressable, such that the phase and amplitude of the source can be modified by an applied voltage. This dynamic reconfigurability necessitates the integration of a control layer within the RF aperture, introducing control devices at each radiating node along with separate bias lines that must be appropriately isolated from the RF signals. Phased arrays and electronically scanned antennas (ESAs) have traditionally made use of semiconductor-based phase shifters and amplifiers—active devices that require external power to achieve their function. Implementation of these devices in planar arrays is already a challenging task; implementing the active devices in a conformal array leads to far greater challenges, given that standard multilayer printed circuit board (PCB) fabrication cannot be directly applied. Moreover, the combination of RF and electronic circuits, as well as the additional active components,

generally leads to a higher profile structure not easily adapted to the curved geometries of interest.

System Calibration: Once the conformal array antenna has been designed and fabricated, it is desirable to perform a calibration to ensure that the system operates as expected. This entails confirming that each of the radiating elements adds the correct phase and amplitude to the incident feed waves. For arrays with hundreds or even thousands of elements, the task can be significant. Since this information is required over the entire frequency band of operation, and possibly over a range of operating temperatures and other conditions, system calibration can consume tremendous resources.

At the outset of this program, we proposed metasurface antennas as a conformal array antenna platform. The inherent properties of metasurface antennas make them easily adaptable to conformal geometries, both in terms of analysis as well as implementation. In particular, metasurface antennas make use of simple, passive components—such as diodes or varactors—to achieve desired reconfigurability. Such components vastly reduce the electrical complexity of the control layer, reduce power consumption requirements, and reduce the need for co-designed thermal management [4]. The elimination of the Tx/Rx (transmit/receive) modules associated with ESAs motivates the introduction of a microwave feed structure, with the metamaterial elements coupling to the guided wave and radiating a portion of the energy. The absence of a local power source at each node (provided by a high-power amplifier in the case of ESAs) means that all power must initially be provided to the waveguide by the RF power source, with each of the metamaterial elements passively coupling the energy to the radiated field—similar to the operation of a traveling wave antenna. To date, planar metasurface antennas have been demonstrated for many different microwave applications, including microwave imaging [5], and are now in the advanced stages of commercialization by several companies [6].

The program was divided into four thrusts to address the key challenges identified for metasurface based conformal array antennas. The main contribution of this work was expected to be a comprehensive modeling, design and characterization approach to conformal metasurface antennas, with some proof-of-concept experiments used to illustrate the methods and tools developed. Since our team had extensive experience in modeling and fabricating planar waveguide-fed metasurface antennas, we decided to focus on this specific architecture as the fastest path to demonstrate the key goals of the program.

The waveguide-fed metasurface antenna can be modelled as an array of polarizable dipoles, with the scattering and radiating properties of each metamaterial element contained within the electric and magnetic polarizability tensors. Since the metamaterial elements are subwavelength in size (roughly a tenth to a sixth of the wavelength), this dipole approximation is appropriate and has been shown to be accurate. The operation of the metasurface antenna can then be understood approximately as the waveguide mode fields exciting each of the metamaterial elements, with the resulting radiation pattern found by summing over the fields radiated by the array of dipoles. The polarizability, which determines the phase and magnitude of the field

radiated by the dipole, is best determined using a full-wave simulator so that arbitrary geometries and materials can be considered. The full-wave simulations are thus performed over a relatively small computational domain, with the remainder of the calculation performed using the relatively simple and fast dipole summation. The result is that very large arrays can be modeled quickly, efficiently and accurately through this multiscale modeling approach.

Since the complexity of the actual geometry is reduced to a sum over dipole radiators, large arrays can be modeled with no requirement of symmetry or periodicity. The dipoles need not be positioned in a regular or even a planar array, but rather can be positioned throughout space in arbitrary arrangements. With this modeling approach, we expected that conformal metasurface arrays could be readily designed.

While the above description provides the conceptual modeling approach, it omits the complications of interaction between the polarizable dipoles and the waveguide mode as well as mutual coupling among the polarizable dipoles. Fortunately, these effects are easily introduced using a coupled-dipole formalism that can account for these effects. The coupled-dipole formalism results in a matrix equation for the polarizabilities (or, equivalently, the dipole moments) in terms of the incident waveguide field, so that a single matrix inversion is needed to arrive at a complete, self-consistent model. The coupled dipole formalism enables us to move beyond the predictions of directivity and radiation patterns, to efficiency, gain, reflection and other crucial antenna parameters. As part of the work in this program, we pursued the modifications needed to apply the dipole and coupled-dipole modeling frameworks to conformal metasurface array antennas.

From the full-wave simulation of a given metamaterial element, the polarizability tensor can be extracted using methods developed by the team. Then, the radiated field can be determined by summing the fields radiated from each of the effective dipoles along the antenna surface. The model is conceptually simple, but operationally somewhat more complicated since the dipoles can interact with each other via free space interactions as well as through the waveguide structure. These interactions can be taken into account in a straightforward and computationally tractable manner using a coupled dipole formalism, which amounts to solving a matrix of dimension roughly on the order of the number of radiating dipoles. For conformal antennas, the change (if any) to the waveguide fields relative to a straight (unbent) waveguide must be accounted for, as well as the fields radiated into the waveguide structure by the dipoles (i.e., equivalently, the Green's function). Thus, the modeling tasks in this first year have been structured so as to first assess the impact of the waveguide bending and then to accurately include the effects in the coupled dipole framework. Once this modeling component is complete, the goal is to demonstrate the entire design process by producing a conformal antenna sample whose properties are accurately predicted using the developed techniques.

Task I.1: Conformal Metasurface Antenna Design

The goal of Task I.1 was to arrive at an initial plan for the conformal antennas to be analyzed and tested later in the program. The initial metasurface array antenna design assumed the simplistic dipole model, ignoring interactions between the metamaterial elements and the waveguide feed as well as interactions. During the first year, a variety of structures were considered, with the final selection being the substrate-integrated waveguide (SIW) structures fabricated using multilayer printed circuit board (PCB) techniques. The SIW geometry is attractive because the waveguide fields are fully confined and analytically described. The SIW-PCB metasurface antenna is quite thin and can be fabricated with substrates that are flexible enough to bend. Though not pursued in this limited study, PCB metasurface antennas can likely be integrated into composites and used to create structural components with appropriate aerodynamic properties while supporting advanced electromagnetic functionality.

As described in the previous section, the dipole model in the absence of interactions is simple and quick to apply, and often gives a good idea of the expected best possible performance of the antenna. The assumptions are that the waveguide mode is unperturbed and that the metamaterial elements behave a simple, polarizable dipoles. As the planar antenna is curved, the positions of the radiating metamaterial elements change, but this effect is easily accounted for by shifting the positions of the equivalent dipoles. Moreover, if the waveguide mode is negligibly perturbed, then the analysis used for the planar structure is trivially modified for the conformal structures. While one of our tasks in Thrust II was to fully solve the waveguide mode in a curved structure, we opted to perform an early numerical study to determine empirically if there were any severe effects on the waveguide mode when a structure was bent.

During the first reporting period, we performed an initial set of numerical experiments with an SIW-PCB type structure. In these numerical experiments, curved waveguide metasurface structures were simulated using full-wave solvers (CST Microwave Studio) to assess the effect of curvature of the waveguide-feed on the guided wave fields within the device. In these studies, the S-parameters of the waveguide feed as a function of frequency were computed for waveguides with different bend radii. A typical SIW-PCB architecture was studied, shown in Fig. 1a, which consists of a rectangular waveguide with two end launches for excitation and termination. The bend radius is swept from 60 mm to 600 mm (Fig. 2a, right), while the corresponding S-parameters are shown in Fig. 2b. Only a minor change in the S-parameters is observed for the various radius of curvatures, indicating that the guided mode is not perturbed significantly by the bend.

These results provided useful evidence that, except for the cases of relatively sharp bends, the fields associated with the waveguide modes determined for a planar structure are not significantly modified when that structure is bent. These studies provided the team with enough confidence to select the SIW PCB architecture as the test platform for this program. Given the computational constraints of full wave simulations, only a relatively small sample could be feasibly studied. A rigorous study of the waveguide mode was still warranted, since for very large

apertures small local errors could accumulate and have greater significance in the composite structure. For this reason, the team developed analytical and quasi-analytical treatments to account for waveguide curvature, as described in Task II.1.

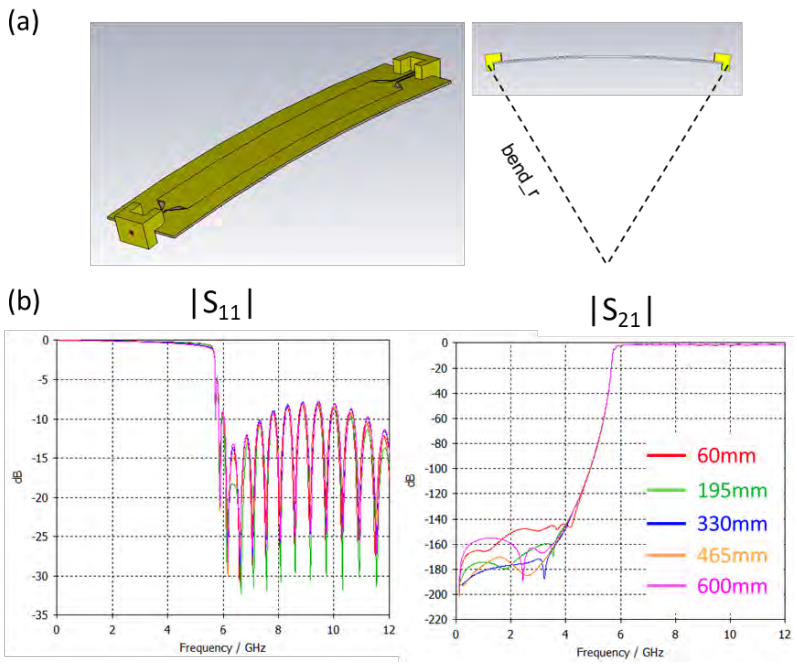

Figure 1 | (a) Schematic of a rectangular waveguide fed by two end launches at the ends. (b) The magnitude of $|S_{11}|$ and $|S_{21}|$ as a function of frequency.

Task II.1: Analyze the Dispersion and Electromagnetic Modes of a Conformal Waveguide

To tackle the problem of solving for the fields exactly in a conformal waveguide structure, the team has pursued two approaches. The first method involves the application of a conformal mapping technique to obtain an exact solution for a specific type of curved waveguide. The second is a perturbative method that is broadly applicable to conformal waveguide-fed metasurface antennas. As described in Task I.1, the exact solution is important to determine if and when the planar waveguide solutions can be applied to the conformal waveguides, and provides an exact solution where the planar approximation fails.

Conformal Mapping Technique

In the first report period, our team developed a method of calculating the radiation patterns from a conformal, waveguide-fed metasurface antenna. The method is based on conformal mapping and transformation optics, in which the coordinate transformation can be equivalently cast in terms of a spatially varying medium inside an otherwise planar waveguide. Fig. 2 (left) shows a general conformal structure and the non-curved equivalent with a spatially varying medium. On the right, a mapping is shown between a straight, rectangular hollow waveguide and a curved waveguide.

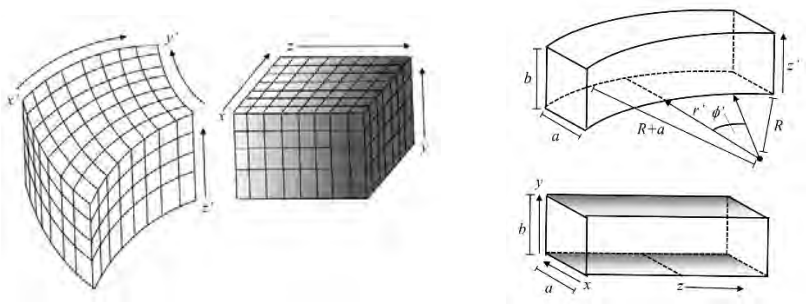

Figure 2 | (left) Illustration of a mapping between an arbitrary coordinate system and a rectangular coordinate system. (right) Mapping of a planar and curved waveguide.

As an example, a curved waveguide, which could, for example, be a leaky-wave antenna placed over a surface, can be simplified to a straight waveguide for which solutions are far easier to analyze. Using this method, a complicated structure on a curved surface can be mapped to a flat one with a virtual, spatially varying medium that replicates the behavior of the curved field in the straight structure. As straight structures are much easier to analyze, the fields may be found in the straight structure and then mapped back to the parent curved structure. The technique can be applied to a curved waveguide, where the planar waveguide filled with a spatially varying dielectric material is much easier to analyze as compared to existing curved waveguide mathematical solutions. Though limited to certain forms of structures, the conformal mapping method is a useful analysis tool that enables assessment of the impact of bending on waveguide modes.

This work was completed during the first reporting period and the details were written into an extensive manuscript, currently still under review in *IEEE Transactions on Antennas and Propagation*. The results show that while the effect of waveguide curvature on the fields is modest, it can nevertheless be quantified and will make a difference for obtaining accurate predictions of radiation patterns from the structure.

Perturbative Approach

The calculation of the radiation pattern of a waveguide backed metamaterial antenna requires the knowledge of the Green's functions for each of the radiating metamaterial elements. While these Green's functions are the well-known Hankel functions in the case of a flat waveguide, the situation is more complex for an arbitrarily shaped waveguide, with the Green's function for every element being generally distinct. Considering the number of elements involved in a full size antenna and its size, it is impractical to run a full wave simulation for every element to determine the information needed to compute the fields from the entire structure.

During the first reporting period, the Northrop group determined to formulate a perturbative approach that would be suitable for finding the guided waves of arbitrarily curved structures. As shown in Fig. 3, the process involves a three-step approach to make calculations tractable: (1) the use of transformation optics to convert the three-dimensional (3D) problem into a 2D

problem; (2) the use of a beam propagation method (BPM) to calculate the Green's functions; and (3) the use of the coupled dipole method (CDM) to calculate the total field inside the waveguide, and ultimately the radiation pattern.

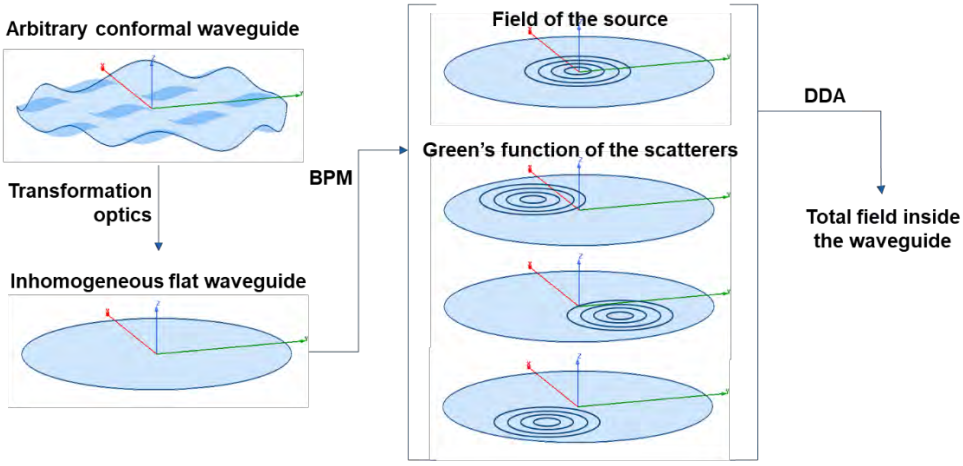

Figure 1 — Schematic representation of our approach. See text for details.

Figure 3 | Schematic representation of the perturbative technique to find the field inside of a conformal waveguide.

Here we show first how we adapt the BPM to cylindrical waves. Then we show how to apply the BPM to a conformal waveguide through an appropriate transform. Finally, we discuss how to use the Green's functions in combination with the CDM to calculate the total field inside the conformal antenna. The basic framework of the technique was developed during the first reporting period, with the actual implementation occurring during the present reporting period.

Calculation of Green's functions inside an inhomogeneous waveguide

To calculate the Green's function inside a parallel plate waveguide, we need to solve the wave equation in cylindrical coordinates,

$$\frac{\partial^2 E_z}{\partial \rho^2} + \frac{1}{\rho}\frac{\partial E_z}{\partial \rho} + \frac{1}{\rho^2}\frac{\partial^2 E_z}{\partial \phi^2} = -\beta^2 E_z.$$

Following the approach used by the standard BPM, the electric field inside the waveguide, E_z, can be expressed as

$$E_z = A(\rho, \phi) E_z^{(0)}$$

where $E_z^{(0)}$ is the known solution for a flat waveguide, while $A(\rho, \phi)$ is a slowly varying envelope. Furthermore, the square of the propagation constant, β, can be separated according to

$$\beta^2 = \beta_0^2 + \Delta\beta^2$$

where β_0 is the propagation constant in the uniform flat waveguide, while $\Delta\beta$ is a perturbation.

Inserting this solution in the wave equation and grouping similar terms gives

$$A(\rho,\phi)\left(\frac{\partial^2 E_z^{(0)}}{\partial\rho^2}+\frac{1}{\rho}\frac{\partial E_z^{(0)}}{\partial\rho}+\frac{1}{\rho^2}\frac{\partial^2 E_z^{(0)}}{\partial\phi^2}\right)+\left(\frac{\partial^2 A(\rho,\phi)}{\partial\rho^2}+\frac{1}{\rho^2}\frac{\partial^2 A(\rho,\phi)}{\partial\phi^2}\right)E_z^{(0)}$$
$$+2\frac{\partial A(\rho,\phi)}{\partial\rho}\frac{\partial E_z^{(0)}}{\partial\rho}+\frac{1}{\rho}A(\rho,\phi)\frac{\partial E_z^{(0)}}{\partial\rho}+\frac{2}{\rho^2}\frac{\partial A(\rho,\phi)}{\partial\phi}\frac{\partial E_z^{(0)}}{\partial\phi}=-(\beta_0^2+\Delta\beta^2)A(\rho,\phi)E_z^{(0)}.$$

The content of the first parenthesis is the left-hand side of the wave equation for the uniform flat waveguide, which, by definition, is equal to $-\beta_0^2 E_z^{(0)}$. Therefore, those terms can be eliminated on both sides. Furthermore, if the envelope is slowly varying, the second order derivative, $\partial^2 A(\rho,\phi)/\partial\rho^2$, is negligible, leading to

$$\frac{1}{\rho^2}\frac{\partial^2 A(\rho,\phi)}{\partial\phi^2}E_z^{(0)}+2\frac{\partial A(\rho,\phi)}{\partial\rho}\frac{\partial E_z^{(0)}}{\partial\rho}+\frac{1}{\rho}A(\rho,\phi)\frac{\partial E_z^{(0)}}{\partial\rho}+\frac{2}{\rho^2}\frac{\partial A(\rho,\phi)}{\partial\phi}\frac{\partial E_z^{(0)}}{\partial\phi}$$
$$=-\Delta\beta^2 A(\rho,\phi)E_z^{(0)}.$$

This differential equation can be further simplified by expressing the envelope function, the field in the uniform waveguide, and the perturbation to the propagation constant as Fourier series according to

$$A(\rho,\phi)=\sum_{m=-\infty}^{+\infty}a_m(\rho)e^{im\phi},\ E_z^{(0)}=\sum_{n=-\infty}^{+\infty}e_n(\rho)e^{in\phi},\ \text{and}\ \Delta\beta^2=\sum_{p=-\infty}^{+\infty}\beta_p(\rho)e^{ip\phi}.$$

Inserting these series in the previous equation, and dropping the explicit ρ dependency for compactness gives

$$\sum_{m,n}\left(-\frac{m^2+2mn}{\rho^2}a_m e_n+2a_m' e_n'+\frac{1}{\rho}a_m' e_n\right)\exp i(m+n)\phi$$
$$=-\sum_{m,n,p}a_m e_n\beta_p\exp i(m+n+p)\phi.$$

The complex exponentials are orthogonal, so that integrating both sides of the above equation over φ leads to an infinite series of coupled differential equations that can be expressed in matrix form as

$$\begin{bmatrix} \vdots \\ a'_{-1} \\ a'_0 \\ a'_{+1} \\ \vdots \end{bmatrix} = \begin{bmatrix} \ddots & \vdots & \vdots & \vdots & \iddots \\ \cdots & e'_0 + \frac{1}{\rho}e_0 & e'_{-1} + \frac{1}{\rho}e_{-1} & e'_{-2} + \frac{1}{\rho}e_{-2} & \cdots \\ \cdots & e'_{+1} + \frac{1}{\rho}e_{+1} & e'_0 + \frac{1}{\rho}e_0 & e'_{-1} + \frac{1}{\rho}e_{-1} & \cdots \\ \cdots & e'_{+2} + \frac{1}{\rho}e_{+2} & e'_{+1} + \frac{1}{\rho}e_{+1} & e'_0 + \frac{1}{\rho}e_0 & \cdots \\ \iddots & \vdots & \vdots & \vdots & \ddots \end{bmatrix}^{-1} \begin{bmatrix} \vdots & \vdots \\ \sum_{m+n+p=-1} a_m e_n \beta_p + & \sum_{m+n=-1} \frac{m^2+mn}{\rho^2} a_m e_n \\ \sum_{m+n+p=0} a_m e_n \beta_p + & \sum_{m+n=0} \frac{m^2+mn}{\rho^2} a_m e_n \\ \sum_{m+n+p=+1} a_m e_n \beta_p & \sum_{m+n=+1} \frac{m^2+mn}{\rho^2} a_m e_n \\ \vdots & \vdots \end{bmatrix},$$

where the subscripts on the sums must be understood as all combinations of m and n, or m, n and p that gives the stated sum.

Assuming that all the Fourier series converge, a finite number of equations can be selected, and the solution can be obtained using a numerical ordinary differential equation solver. In this work, we have implemented our approach in Matlab, and used the solvers that it provides. One interesting observation is that the matrix that needs to be inverted only depends on the known solution inside the homogeneous waveguide. The source of the field is usually an electric or a magnetic dipole, or can be decomposed as a combination of those. Therefore the known solution only has a small number of terms and the matrix is band diagonal. If the source is an electric dipole in z,

$$E_z^{(0)} \propto H_0^{(2)}(\beta_0 \rho)$$

containing only a single term for $n = 0$, the Hankel function of 0th order. If the source is a magnetic dipole in the plane of the waveguide,

$$E_z^{(0)} \propto H_{-1}^{(2)}(\beta_0 \rho) e^{-i\phi} \pm H_{+1}^{(2)}(\beta_0 \rho) e^{+i\phi}$$

containing only two terms, the Hankel functions of positive and negative 1st order. The sign of the sum depends on whether the magnetic dipole is polarized along the x or the y axis. The small number of terms can also be used to speed up the calculation of the sums by noting that most combinations are null.

Example: Graded-Index Lens

We now illustrate the approach with a simple example, that of a graded-index lens with a source at the origin inside a parallel plate waveguide, illustrated in Fig. 4. The thickness of the waveguide is selected to be small enough such that only the fundamental mode is supported. This mode is TEM and the propagation constant is the same as that of a plane wave in the same material, as shown in Fig. 4(a).

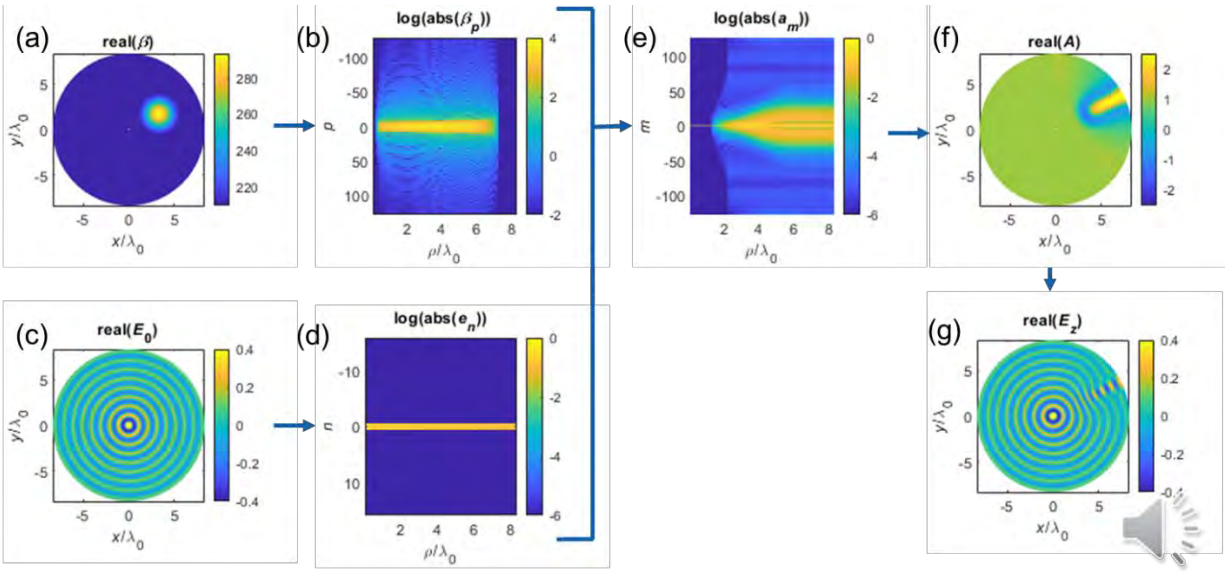

Figure 4 | Calculation of the fields inside a parallel plate waveguide filled with a graded-index lens.

The first step is to calculate the Fourier components of the propagation constant as a function of ρ, shown in Fig. 4(b). A finite number of terms are retained in this step; the number of terms that should be kept depends on the complexity of the propagation constant profile, as well as the distance over which the field needs to be propagated. For a given problem, the higher the number of terms the better the solution, but at the cost of longer computation. Here we selected 256 terms.

Note that the values of all the Fourier components are typically complex, and that only their absolute values are shown in Fig. 4.

In parallel, we need the solution for the homogeneous waveguide. As mentioned above, this solution is a Hankel function, illustrated in Fig. 4(c), whose Fourier series consists of a single term independent of ρ, as shown in Fig. 4(d).

At the origin, the envelope is equal to 1, and its Fourier series has a single term. Inserting this initial condition inside the differential equation solver and iterating over the values of ρ, the Fourier components of the envelope function are calculated over the whole waveguide, as shown in Fig. 4(e). After the Fourier components have been calculated, the envelope function in real space is calculated, as shown in Fig. 2(f).

Finally, the value of the field inside of the waveguide is obtained by multiplying the known solution for the homogeneous waveguide with the envelope function, as shown in Fig. 4(g).

It should be noted that, in reality, the Fourier components of the propagation constant and the known solution for the homogeneous waveguide are not computed in advance. The differential equation solver automatically adjusts the ρ step size to minimize the number of steps while

providing the desired accuracy. It is therefore impossible to know beforehand the values of ρ where β_p and e_n are needed and these are calculated on the fly.

Application to Conformal Waveguides

Now that we have adapted the BPM to calculate the perturbed cylindrical waves inside an inhomogeneous parallel plate waveguide, we show how to apply it to a parallel plate waveguide with an arbitrary shape, like the one that would be used in a conformal antenna.

A flat waveguide equivalent to an arbitrary shaped waveguide can be obtained by transformation optics. In the equivalent waveguide, the permittivity and the permeability are

$$\epsilon' = \frac{AA^T}{|A|}\epsilon, \quad \mu' = \frac{AA^T}{|A|}\mu.$$

where A is the Jacobian of the transformation [7].

The particular transform depends on the specific geometry. One general class of conformal waveguide that we have tested is the one where the middle of the waveguide is defined by

$$z_{\text{middle}} = f(x', y'),$$

where the primed coordinates are the coordinates of the original conformal waveguide. Unfortunately, the transform of such a waveguide does not have an analytical solution. It is possible to obtain an analytical solution assuming $f(x', y') \approx f(x, y)$, where the unprimed coordinates are those of the equivalent flat waveguide. An example of such a transform is shown in Fig. 5 for

$$f(x, y) \approx f(x', y') = h \sin\frac{2\pi x}{\Lambda_x} \cos\frac{2\pi y}{\Lambda_y}.$$

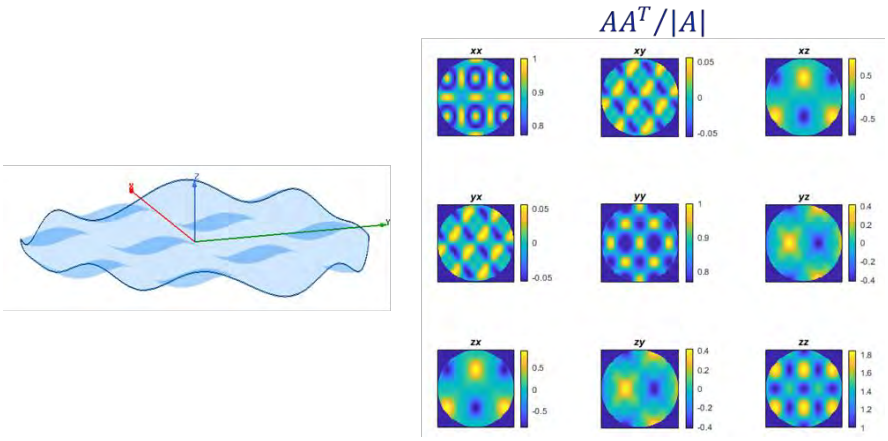

Figure 5 | Approximate transform (right) of a conformal waveguide (left) defined by separable trigonometric functions in x and y.

Despite the apparent simplicity of the approximate transform just described, the analytical formula is extremely long (we don't show it here as it would take many pages). It is sufficiently involved to actually slow down the calculations. Since our goal is to develop a fast approach, the BPM is an approximation, and the transform we just described is also an approximation, we feel justified to use a more empirical transform. Specifically, we assume that inside the equivalent flat waveguide

$$\beta(\vec{k}) = \beta_0 \nabla_{xy} f \cdot \vec{k}/|\vec{k}|$$

where $\vec{k}$ is the local wavevector in the equivalent flat waveguide. This effectively normalizes the propagation constant by the ratio of the wavevector in the conformal waveguide and its projection in the equivalent flat waveguide. For the moderate deformations that can be solved by the BPM, this gives good results.

One difficulty that arises when using either the transformation optic properties, or the empirical ones, is that the propagation constant is anisotropic. It is necessary to know the local direction of propagation of the wave to determine the propagation constant. However, this local direction is not known before the solution at a given position is calculated. In this context, the system of differential equations is implicit, and a solver specialized for this type of problem must be used. Interestingly, we have found the Matlab's implicit solver gives faster results even when applied to isotropic problems like the one presented in the previous section.

The local propagation constant is the gradient of the phase of the field. In cylindrical coordinates,

$$\vec{k} = \frac{\partial \arg E_z}{\partial \rho}\hat{\rho} + \frac{1}{\rho}\frac{\partial \arg E_z}{\partial \phi}\hat{\phi},$$

where

$$\frac{\partial \arg E_z}{\partial \rho} = \operatorname{imag}\left(\frac{1}{E_z}\frac{\partial E_z}{\partial \rho}\right), \quad \frac{\partial \arg E_z}{\partial \phi} = \operatorname{imag}\left(\frac{1}{E_z}\frac{\partial E_z}{\partial \phi}\right),$$

$$\frac{\partial E_z}{\partial \rho} = \sum_m a_m(\rho)e^{im\phi}\sum_n e_n'(\rho)e^{in\phi} + \sum_m a_m'(\rho)e^{im\phi}\sum_n e_n(\rho)e^{in\phi}, \text{ and}$$

$$\frac{\partial E_z}{\partial \phi} = \sum_m a_m(\rho)e^{im\phi}\sum_n ine_n(\rho)e^{in\phi} + \sum_m ima_m(\rho)e^{im\phi}\sum_n e_n(\rho)e^{in\phi}.$$

Fig. 6 shows the phase, local propagation direction, and electric field inside a flat waveguide equivalent to the conformal waveguide defined above for $h = 4\lambda_0/3$, $\Lambda_x = 5\lambda_0$, and $\Lambda_y = 20\lambda_0/3$, where λ_0 is the free space wavelength of the considered wave.

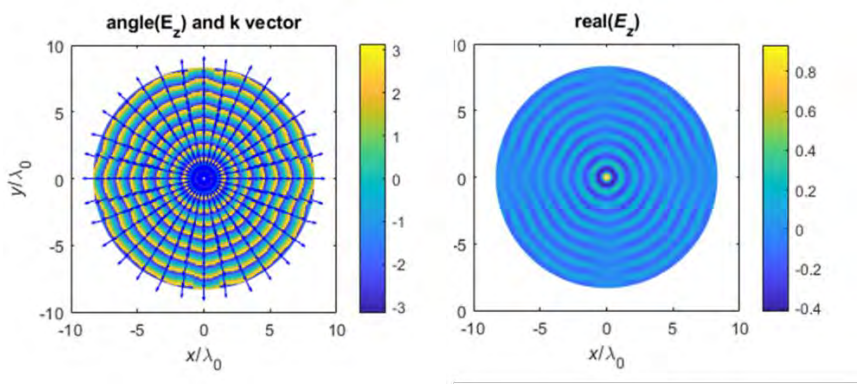

Figure 6 | Phase and local propagation constant (left) and electric field (right) of the wave generated by an electric dipole at the origin, inside a flat waveguide equivalent.

Integration with the Coupled Dipole Method (CDM)

A conformal waveguide-backed metamaterial antenna consists of a large number of metamaterial elements in one of the conductors of the waveguide. The fields inside the waveguide can be calculated using the CDM, where we suppose that the field at any of the elements is the sum of the applied field and those generated by the other elements, which are initially unknown. This problem is expressed as the linear system of equations

$$\begin{bmatrix} \bar{\bar{\alpha}}_1^{-1} & \bar{\bar{G}}_{12} & \cdots \\ \bar{\bar{G}}_{21} & \bar{\bar{\alpha}}_1^{-1} & \cdots \\ \vdots & \vdots & \ddots \end{bmatrix} \begin{bmatrix} \vec{p}_1 \\ \vec{p}_2 \\ \vdots \end{bmatrix} = \begin{bmatrix} \vec{F}_1 \\ \vec{F}_2 \\ \vdots \end{bmatrix},$$

where $\bar{\bar{\alpha}}_i$ are the polarizabilities of the elements, $\bar{\bar{G}}_{ij}$ are the Green's functions, $\vec{p}_j$ are the polarizations and magnetizations of the elements, and $\vec{F}_i$ are the applied fields. For the parallel plate waveguide, the electric field is polarized in z while the magnetic field is in the plane. Therefore, it is only necessary to consider those elements of the fields, the polarizabilities, the Green's functions, and the polarizations and magnetizations. Specifically, in the absence of magnetoelectric effects in the elements,

$$\bar{\bar{\alpha}}_i = \begin{bmatrix} \alpha_z^{(e)} & 0 & 0 \\ 0 & \alpha_x^{(m)} & 0 \\ 0 & 0 & \alpha_y^{(m)} \end{bmatrix}_i, \quad \bar{\bar{G}}_{ij} = \begin{bmatrix} G_{zz}^{ee} & G_{zx}^{em} & G_{zy}^{em} \\ G_{xz}^{me} & G_{xx}^{mm} & G_{xy}^{mm} \\ G_{yz}^{me} & G_{yx}^{mm} & G_{yy}^{mm} \end{bmatrix}_{ij}, \quad \vec{p}_j = \begin{bmatrix} p_z \\ m_x \\ m_y \end{bmatrix}_j, \text{ and } \vec{F}_i = \begin{bmatrix} E_z \\ H_x \\ H_y \end{bmatrix}_i.$$

The Green's functions as well as the applied fields are calculated using the BPM with the source for an electric or magnetic dipole mentioned above.

Up to this point we have only seen how to calculate the electric field. To calculate the magnetic field, and the corresponding elements of the Green's function tensor, the electric field is calculated first, and then the magnetic field is calculated from the gradient of the electric field.

Fig. 7 shows typical results. Note that the Green's functions are different from those of a flat waveguide. For example, G_{zz}^{ee} looks square, while it would be perfectly circular for a flat waveguide.

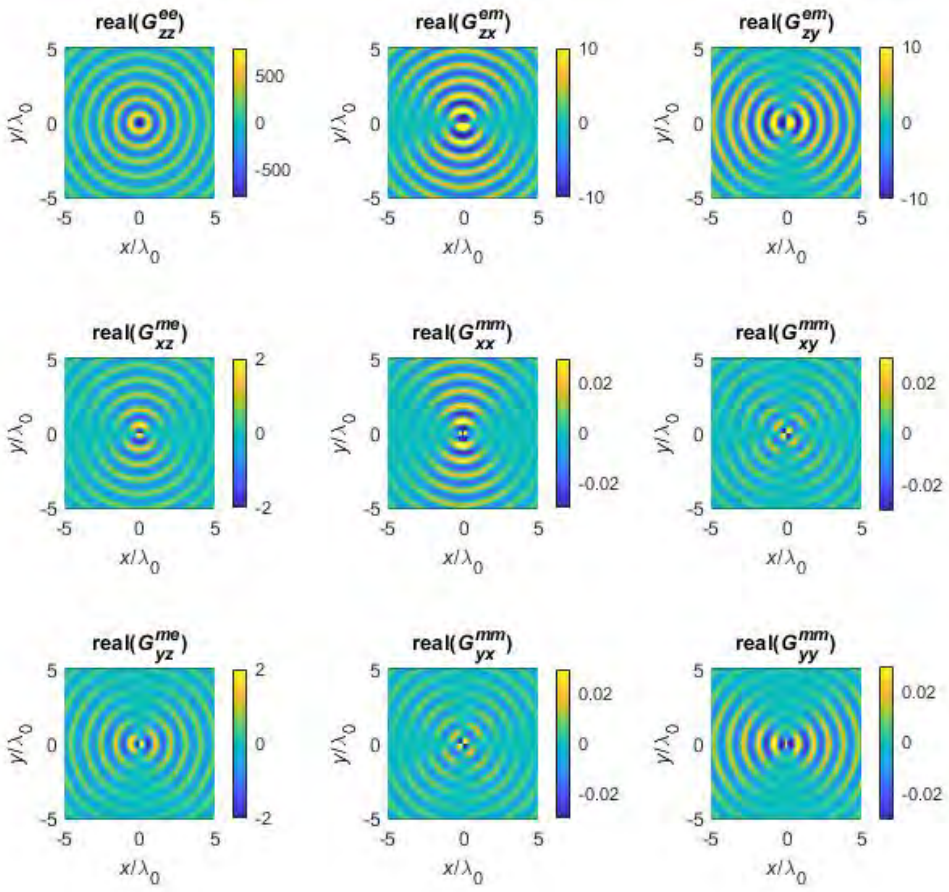

Figure 7 | Green's function of an element located at the origin for $\boldsymbol{h = \lambda_0/3}$, $\boldsymbol{\Lambda_x = 5\lambda_0}$, and $\boldsymbol{\Lambda_y = 20\lambda_0/3}$.

The electric and magnetic polarizabilities, $\alpha_z^{(e)}$, $\alpha_x^{(m)}$, and $\alpha_y^{(m)}$ can be determined analytically for some simple geometries, or can be determined from simulations in general, as shown in Fig. 8. There, a plane wave excites a flat parallel plate waveguide with a circular aperture (we assume that the polarizabilities are not strongly affected by the deformation of the waveguide). Using the Green's functions calculated above, we fit the fields as the sum of the applied fields and those scattered by the elements.

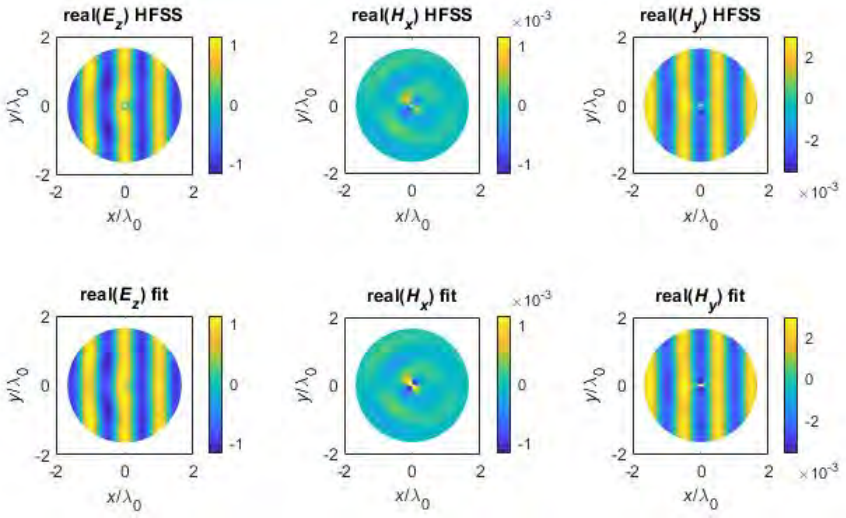

Figure 8 | Fitted simulation to determine the electric and magnetic polarizabilities of circular apertures.

The last step is putting all the approaches discussed together to calculate the field inside a conformal waveguide. Fig. 9 shows the field inside a waveguide fed from the center with five scatterers, as calculated using our approach and using HFSS. The scatterers are vias connecting to top and bottom conductors. Our approach provides excellent prediction of the phase, and good prediction of the amplitude of the field.

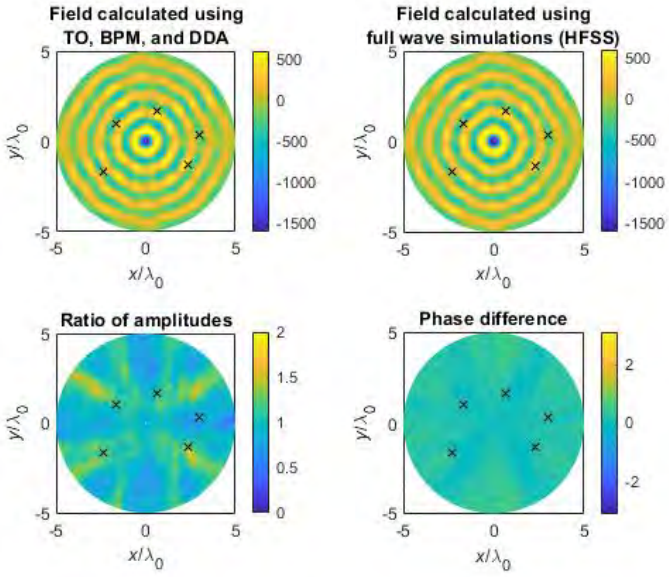

Figure 9 | Simulation of a parallel plate waveguide with five scatterers (indicated by x's) and comparison with HFSS simulation.

The perturbative approach enables the calculation of the field within a conformal waveguide of arbitrary shape, and can be used to confirm the degree to which the fields of the unperturbed planar waveguide are modified.

We note here that we were unable to couple the perturbative technique with a metasurface antenna design during the time of this program. In the work presented in the following tasks, we used large bend radii and assumed that the corrections would be negligible. In the future, we hope to combine the perturbative solutions for structures with smaller bend radii, where the planar approximation breaks down.

Task II.2: Modeling of Tunable Metamaterial Resonators for Conformal SIW and CPW Architectures

During this reporting period, we have significantly extended the coupled dipole modeling approach and adapted it for conformal metasurface antennas. During the previous report period, we expanded the coupled dipole model to include interactions with vias and with the coaxial sources, such that antenna parameters such as gain and efficiency could be determined. We also investigated the degree of coupling between metamaterial elements, arriving empirically at an estimate as to how close the elements can be placed to each other and remain within the dipole approximation. The tasks performed in this reporting period apply the model in the design of a conformal metasurface array.

The coupled dipole formalism results in lengthy expressions that are not worth including here. We have completed a manuscript that details the approaches used and appended it to this report [I. Yoo and D. R. Smith, "Design of conformal array of rectangular waveguide-fed metasurfaces," submitted (2020)].

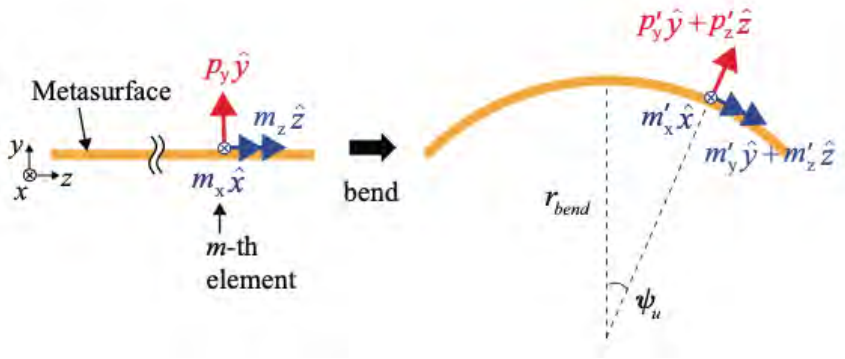

Figure 10 | Schematic of a planar and a cylindrical conformal waveguide-fed metasurface antenna (side view). The metasurface wraps a cylindrical surface (with a radius of r_{bend}) along the circumferential direction.

Dipolar Modeling of Metamaterial Elements

A planar metamaterial element is modeled as a point electric dipole (perpendicular to the plane of the element) and magnetic dipoles (parallel to the plane of the element). If we bend the metasurface to wrap the surface of a cylinder with a radius along the circumferential direction, we suggest that the cylindrical surface can be considered locally piece-wise linear, such that the electric dipole, located at the center of the element, is in the direction normal to the circumference (see Fig. 10). This assumption turns out to hold when the bend radius is large.

Under these assumptions, we can apply the standard polarizability retrieval technique to characterize tunable metamaterial elements embedded in a waveguide wall. Figs. 11(a)-(d) show the schematic of a metamaterial element simulated using a full-wave electromagnetic solver and the extracted polarizabilities as functions of frequency and tuning state.

Tunable metamaterial elements will have similar resonant responses in their polarizabilities, as illustrated in Figs. 11(b)-(d), and thus, they can be well-described using the dipolar modeling approach outlined in this task.

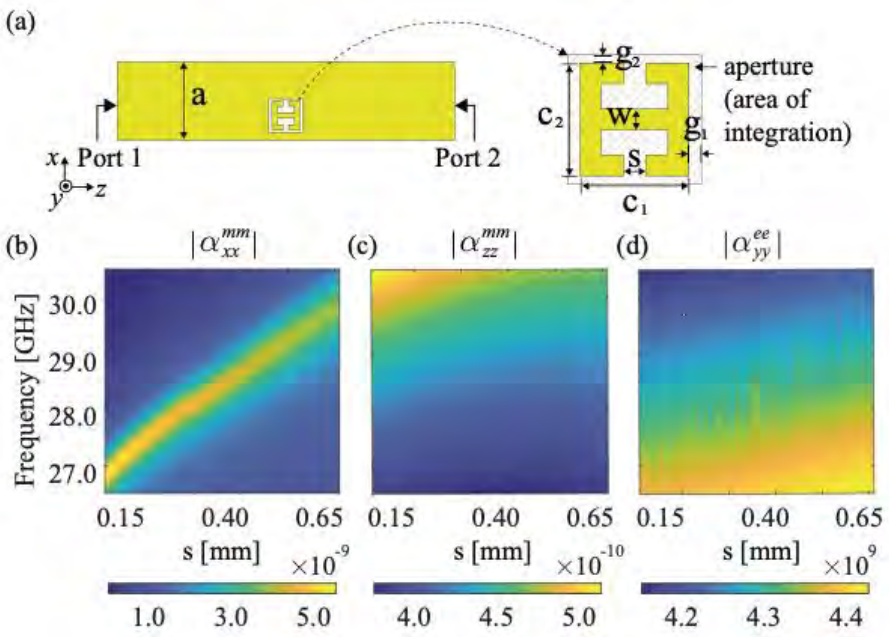

Figure 11 | Simulation setup for the polarizability retrieval. The width of the waveguide is a = 3.41 mm. Orange color indicates perfect electric conductor. Design parameters of the metamaterial elements are c1 = 1.6 mm, c2 = 1.55 mm, g1 =0.15 mm, g2 =0.1 mm, and w=0.25mm. (b)-(d) The amplitude of the polarizability components as functions of frequency and tuning state s.

Task II.3.1: Analysis of Conformal Metasurface Antennas

Advanced Modeling: Coupled Dipole Model

In this task, we continue to extend the coupled dipole framework to conformal metasurface antennas. For planar metamaterial elements, the framework of dipolar modeling of the elements—which is based on the analysis of the electric field on the planar aperture of a small iris—is well studied in literature. Accordingly, a planar metamaterial element with an arbitrary shape can be described as the combination of point electric and magnetic dipoles, so that coupled-dipole methods naturally capture the interactions among the elements. For curved metamaterial elements, however, the electric field at one location on the curved aperture is not always tangential to the element's surface, which does not satisfy the assumption used in the dipolar modeling approach. Therefore, the direct application of the dipolar modeling approach to the curved elements is not straightforward. One can assume the field formed on the aperture to model an element such as a curved slot, but the closed-form expression of the field may not be attainable for complex-shaped metamaterial elements. To remedy such a complex problem, we consider a circumferential rectangular waveguide (or its equivalent SIW) with a large bend radius and assume that the waveguide is piece-wise linear along the circumference of the cylindrical surface. While approximate, we find that such an assumption allows a reasonably accurate description of the curved metamaterial elements using the Green's functions of the dipoles in a flat waveguide. The coupled dipole model can be written as:

$$\begin{bmatrix} \mathbf{G_{11}} & \mathbf{G_{12}} & \cdots & \mathbf{G_{1K}} \\ \mathbf{G_{21}} & \mathbf{G_{22}} & \cdots & \mathbf{G_{2K}} \\ \vdots & \vdots & \ddots & \vdots \\ \mathbf{G_{K1}} & \mathbf{G_{K2}} & \cdots & \mathbf{G_{KK}} \end{bmatrix} \begin{bmatrix} \mathbf{J_1} \\ \mathbf{J_2} \\ \vdots \\ \mathbf{J_K} \end{bmatrix} = \begin{bmatrix} \mathbf{F_1} \\ \mathbf{F_2} \\ \vdots \\ \mathbf{F_K} \end{bmatrix},$$

Where $\mathbf{G_{kk}}$, $\mathbf{J_k}$ and $\mathbf{F_k}$ are the Green's functions, dipole moments representing metamaterial elements, and the incident fields, respectively. By solving the coupled matrix equation above, we can compute the dipole moments representing all of the metamaterial elements in the array system. The far-field can be computed by sum of the radiated fields by the elements. (The matrix equation summarized above hides considerable detail that is provided in the manuscript appended to this report.)

To verify the coupled dipole modeling approach for conformal metasurface antennas, we consider a conformal array of four rectangular waveguide-fed metasurfaces, each with 10 metamaterial elements. The schematic of the designed metasurface before bending is depicted in Fig. 12(a) and after bending is illustrated in Fig. 12(b). The width and height of a cross-section of the waveguide are a = 3.41 mm, b = 0.762 mm. The waveguides are filled with Rogers 4003 circuit board, and their spacing for the unbent structure is 5.0 mm. The metamaterial elements are etched into the curved top plates of the waveguides. The radius of curvature is 111.4 mm, and the arc length is 98.0 mm. We assume the center of the cylindrical surface of the top plate is located at the origin, as indicated in Fig. 12(b).

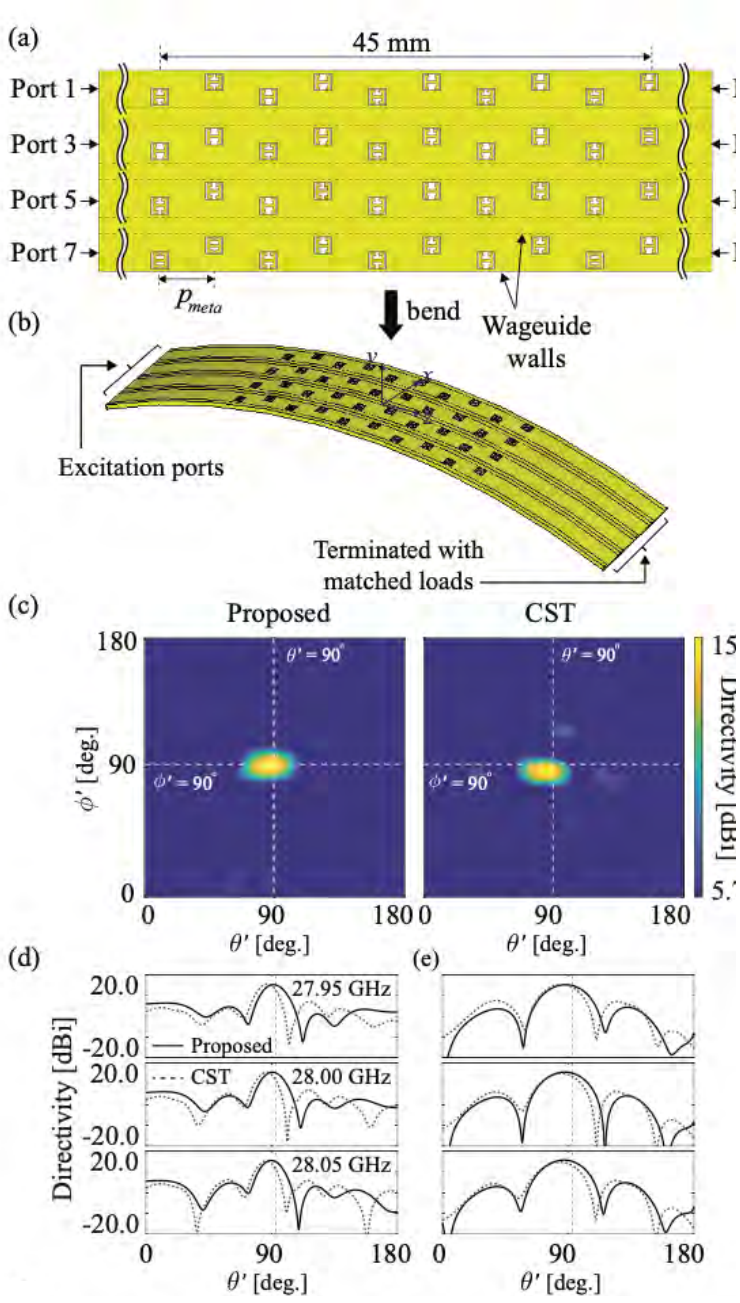

Figure 12 | (a) Schematic of the designed cylindrical, conformal waveguide-fed metasurface antenna before bending (top view). The dotted lines indicate the side walls of each metasurface. (b) Perspective view of the designed metasurface antenna wrapping a cylindrical surface (with a radius of r_{bend}) along the circumferential direction. The arc length is 98 mm. (c) Directivity pattern of the designed conformal metasurface antenna at 28 GHz. (d) The cross-sectional plot of radiation patterns for the swept frequencies (at the plane of θ′ = 90◦).

The designed antenna is verified through the full-wave numerical analysis, where a large perfect conducting, conformal surface with the same radius of curvature is incorporated to suppress the diffraction of the radiated fields at the edges. Fig. 12(c) shows the predicted and simulated directivity patterns at 28.0 GHz, demonstrating good agreement. In the predicted pattern, the main beam is formed at ϕ = 90.3◦, θ = 88.2◦. The main beam of the simulated pattern is at ϕ' = 86.8◦, θ' = 86.8◦, which is slightly offset from the target direction. The predicted and simulated directivity values are 15.7 dBi and 16.0 dBi, respectively. The side lobe level (SLL) of the predicted pattern is computed to be 9.1 dB and that of the simulated pattern is 7.6 dB. To confirm the operating bandwidth of the antenna, we show the cross-sectional plots of the radiation patterns at θ' = 90◦ and ϕ' = 90◦ in Fig. 12(d). As depicted in Fig. 12(d), the shapes of the main beam are maintained over the swept frequencies, and the beams are directed toward the target direction at the swept frequency points, confirming the operation bandwidth of 100 MHz. Although approximate, the studies in Figs. 12 demonstrate that the proposed approach can be used as an effective design tool for the cylindrical conformal array of metasurfaces with a large bend radius.

Task II.3.2: Synthesis of Patterns from Conformal Metasurface Antennas

Pattern Synthesis using an Optimizer

Once having obtained the coupled dipole model for the antenna, the next step is to apply some approach to find an optimal set of polarizabilities that will produce a desired far-field radiation pattern. To obtain the set of available polarizabilities, we analyzed the metamaterial element illustrated in Fig. 13(a) and obtained the polarizabilities by sweeping the gap size from 0.15 mm to 0.65 mm. The extracted polarizabilities as functions of gap size and frequency are shown in Figs. 13(b-d). If we fix the operating frequency f = f_{op}, the obtained polarizabilities of the element can be considered as a function that solely relies on the gap size s (i.e., $\alpha_{xx}^{mm}(f = f_{op}, s)$, $\alpha_{zz}^{mm}(f = f_{op}, s)$ and $\alpha_{zz}^{ee}(f = f_{op}, s)$). We can then consider the gap size of individual elements as a tuning parameter that can be controlled for the design. As we have a multitude of metamaterial elements in the metasurface, the remaining step for the design is equivalent to finding the optimal set of gap sizes s that can achieve the target antenna parameters.

The process of finding the optimal set of gap sizes s can be accelerated by utilizing the analytic model and an effective optimization technique. For the optimization algorithm, we here employ CMA-ES (covariance matrix adaptation evolution strategy), which has been reported to work effectively for the design of metasurfaces (see appended manuscript for details). In our design approach, CMA-ES is integrated with the proposed model to seek the set of gap sizes that minimizes the cost function, defined as

$$cost = -[min(G) + 0.5 \times min(SLL)],$$

with *D* and *SLL* being, respectively, the directivity along the target direction and the sidelobe level (SLL) when the odd-numbered ports are excited simultaneously by feed waves with the same magnitude and phase. The metasurface antenna shown in Fig. 12(b) was designed by using the approach outlined in this subsection.

In the designed conformal metasurface antenna shown in Fig. 12(b), we used a bend radius of r_{bend} = 159.3 mm, which is sufficiently large in terms of the wavelength, i.e., $k_0 r_{bend}$ = 93.3. However, finding the minimum allowed bend radius can provide further insight into the limitation of the proposed design method. Hence, we find the range of allowed bend radius by analyzing the designed conformal antenna with the bend radius r_{bend} swept from 31.8 mm to 191.0 mm. Figure 13 shows the cross-sectional plots of the directivity at θ′ = 90◦ and ϕ′ = 90◦ for the swept bend radius. As shown in Figures 13(b)-(f), the predicted and simulated patterns at θ′ = 90◦ show good agreement. However, the predicted pattern at the plane of ϕ′ = 90◦ exhibits lower side lobe levels near θ′ = 139◦ and starts to deviate from the simulated pattern for k0rbend < 74.7. As shown in Fig. 13 (a), the directivity patterns at both planes are deviated from the simulated patterns, indicating that the minimum allowed bend radius is $k_0 r_{bend} \approx 28$.

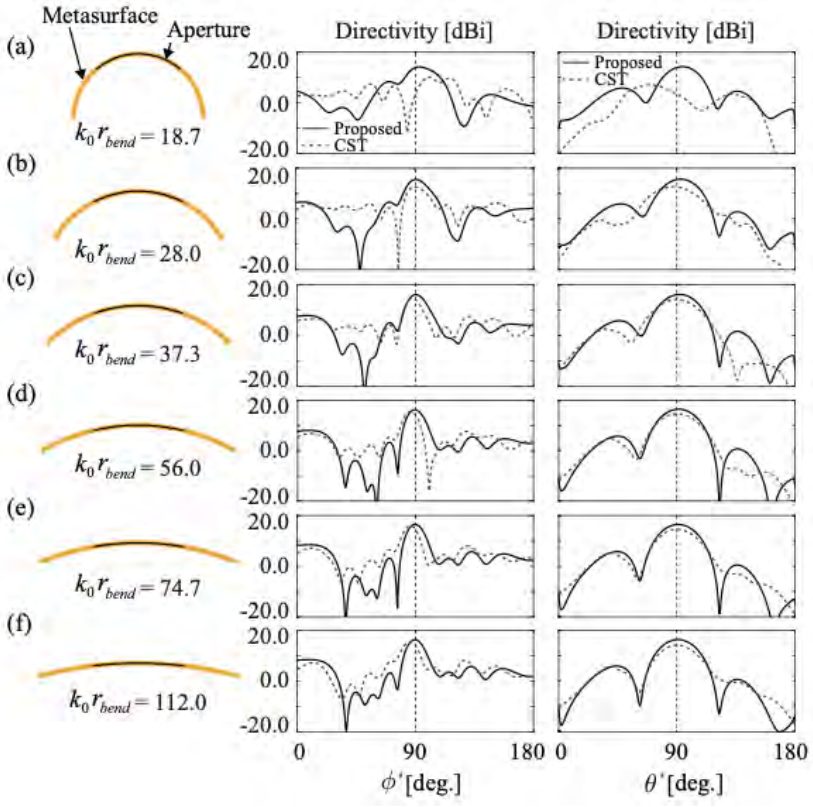

Figure 13 | Side view of the cylindrical conformal waveguide-fed metasurface antenna (left column). The cross-sectional directivity patterns at θ′ = 90◦ (middle column) and at ϕ′ = 90◦ (right column). The directivity patterns are computed at 28.0 GHz. The bend radius r_{bend} is (a) 31.8 mm, (b) 47.7 mm, (c) 63.7 mm, (d) 95.5, (e) 127.3 mm, (f) 191.0 mm.

Task II.4: Design of Feed Structure

Design of Feed Structure for a Conformal Array of Metasurfaces

For the design of a conformal array of metasurfaces, it is required to have an efficient feed structure that can excite the metasurfaces with desired amplitudes and phases. Fig. 14 illustrates an example of such feed structures, where a four-way power divider is used to excite a conformal array of metasurfaces in the middle. Each metasurface in the antenna is terminated with SIW-to-coaxial transition connected with a matched load. In this sub task, we design the feed structures shown in Fig. 14.

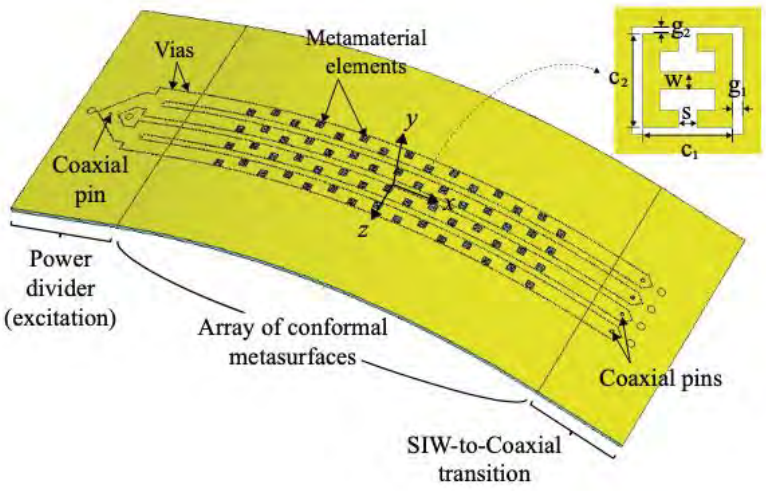

Figure 14 | Schematic of a conformal array of rectangular waveguide-fed metasurface antenna. A four-way power divider is used as a feed network and SIW-to-coaxial transitions are used as terminations. Design parameters of the metamaterial elements are c1 = 1.6 mm, c2 = 1.55 mm, g1 = 0.15 mm, g2 =0.1mm, and w=0.25mm.

Fig. 15(a) shows the top view of the power divider, which is designed to split the input power equally into four separate SIWs with the same phase. In the divider, a coaxial pin is connected to the top conducting plate, and the outer conductor of the coaxial port is connected to the bottom plate. The diameter of the coaxial pin is 0.318 mm. The divider is fed through the coaxial connector, and TEM mode in the coaxial port is converted into TE_{10} mode to feed the SIWs. The power divider is filled with 0.76-mm-thick Rogers 4003 circuit board ($\varepsilon r = 3.55$ and $\tan \delta = 0.0027$). The radius of each via for constructing the SIW is r_{via} = 0.1 mm, and spacing between adjacent vias is d_{via} = 0.5 mm. The dimensions of the vias are chosen such that the SIW is the equivalent of a rectangular waveguide with the same height and width of 3.41 mm. The designed divider was analyzed by using a full-wave electromagnetic solver, CST Microwave Studio. Fig. 15(b) shows the

magnitude of the S-parameters when port 1 is excited. Note that the operating frequency of the divider is 28.0 GHz.

We also designed a SIW-to-coaxial transition, the schematic of which is shown in Fig. 15(c). The designed transition is fed by the coaxial connector, and an annular gap with its width of 0.1 mm is inserted around the coaxial pin. The designed transition was analyzed with the full-wave solver, and the magnitude of S-parameter is shown in Fig. 15(d).

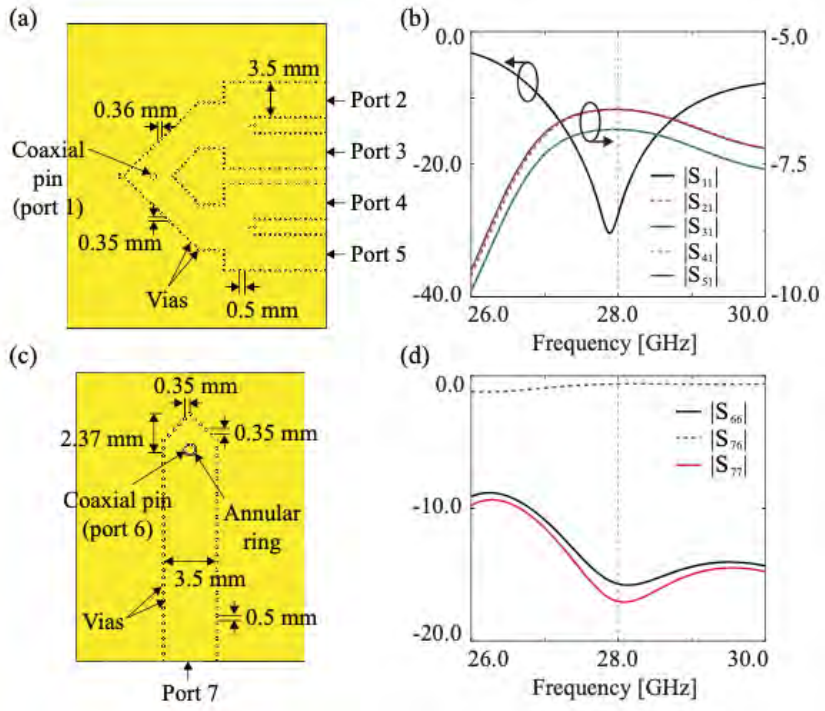

Figure 15 | Schematic of a conformal array of rectangular waveguide-fed metasurface antenna. A four-way power divider is used as a feed network and SIW-to-coaxial transitions are used as terminations. Design parameters of the metamaterial elements are c1 = 1.6 mm, c2 = 1.55 mm, g1 = 0.15 mm, g2 =0.1mm, and w=0.25mm.

THRUST (III): ANTENNA CALIBRATION, OPTIMIZATION AND ORTHOGONALLY CODED NEAR FIELD (OCNF) SCAN DEVELOPMENT

Introduction

The efforts of the University of Washington during this reporting period were focused on Thrust III of the DESI program. The goal of this thrust is to research and develop efficient calibration techniques to allow *in situ* fine tuning of nonconformal metasurface antenna operation. The approach taken is called "Orthogonally Coded Near-Field" (OCNF) where a coded control sequence is applied to the dynamic metasurface aperture (DMA) control elements to enable the efficient, parallelized measurement of the radiated magnitude and phase across a large number of measurement positions in a near field scan. This near field scan data will then be projected

into the far field to yield the radiation pattern of the DMA across the entire range of useful control states. In the past, the standard approach to characterize dynamic metasurface antennas was to take measurements for all possible element state combinations. An important goal of our effort is to leverage a near field measurement of carefully selected set of orthogonally coded measurement states (OCNF) to reduce the number of required measurements, and thus reduce the measurement time dramatically compared with the exhaustive measurement approach.

During the previous report period, the OCNF approach was developed and the theory worked out, with several simulations performed to illustrate the operation of the technique. It was expected that the method would be applied to a larger 1D or possibly 2D array during the current reporting period.

Due to the COVID-19 pandemic, lab access at UW was extremely limited beginning in March 2020 and extending throughout the remainder of the program. UW remained in Phase I and 2a through the work period. Consequently, computer modeling and simulation using previously measured DMA samples (shown in Fig. 16) to form synthetic data sets were used to make progress during this period.

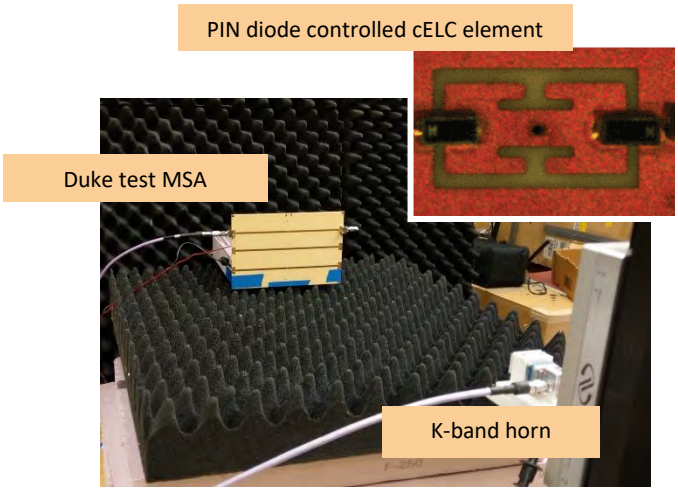

Figure 16 | Single K-band dynamic metasurface element.

Summary of Approach:

As described in the last report, Fig. 16 shows the dynamic metasurface antenna (DMA) element, while Fig. 17 shows the near-field scan (NFS) setup and boresight measurement results for various DMA states of a single DMA element. The NFS setup uses a standard 10 dB gain horn antenna as probe to capture the electromagnetic field emitted by the DMA element. The DMA element is controlled by an Arduino microcontroller which is place behind the DMA antenna. The PIN diode current was controlled by an 8-bit digital to analog converter (DAC) to yield 256 discrete drive voltages ranging from zero to 5 V, corresponding to PIN diode currents from zero to approximately 20 mA. Using a horn-based characterization method, we determined that a 5 bit sub-range (32 control states) was sufficient to encompass the useful tuning range of the DMA element (ie the sub-range where the PIN diode impedance meaningfully affected the radiation

of the DMA element). Thus a single element could be configured with any of those 32 control states, and an *n* element array could be configured with 2^{5n} potential states. For a large array having many elements, the total number of control states rapidly renders the current exhaustive sequential measurement approach extremely time consuming. Thus the OCNF approach seeks to extrapolate the entire array behavior from a parallel measurement of coded control sequences.

The measurement results in Fig. 17 show the magnitude and group delay of the DMA element for some discrete DMA tuning states where the horn antenna was placed directly in front of the DMA element. A vector network analyzer (VNA) was used to obtain these measurements. In a near-field scan, such measurements need to be taken over a 2D raster parallel to the DMA surface with approximately 5 mm steps. As measuring all discrete DMA tuning states for a single 2D scan position took approx. 140 seconds, a full NFS would have taken up to three weeks. As this is an undesirably long measurement time, the measurement setup needed to be optimized, and the number of DMA tuning states needed to be restricted. This was the focus of the work in the final period of the program.

To make this measurement, a simplified setup was constructed that had some of the key features of a conventional near field characterization. A 10dB standard gain horn antenna was used as a probe. Using a horn-to-horn measurement, the response of the horn was first calibrated out. Then, one horn was used to scan the DMA at a distance of approximately 0.5m from the sample. Initially, the horn was located on boresight with respect to the DMA element. Two-port S-parameter measurements (S_{21}) were performed from the DMA to the horn to measure the magnitude and phase response of the radiated field from the DMA. In this experiment, at the single measurement position (boresight) the DMA control current was sequentially set to each of the 32 sub-range control voltages and the measured S-parameters were collected.

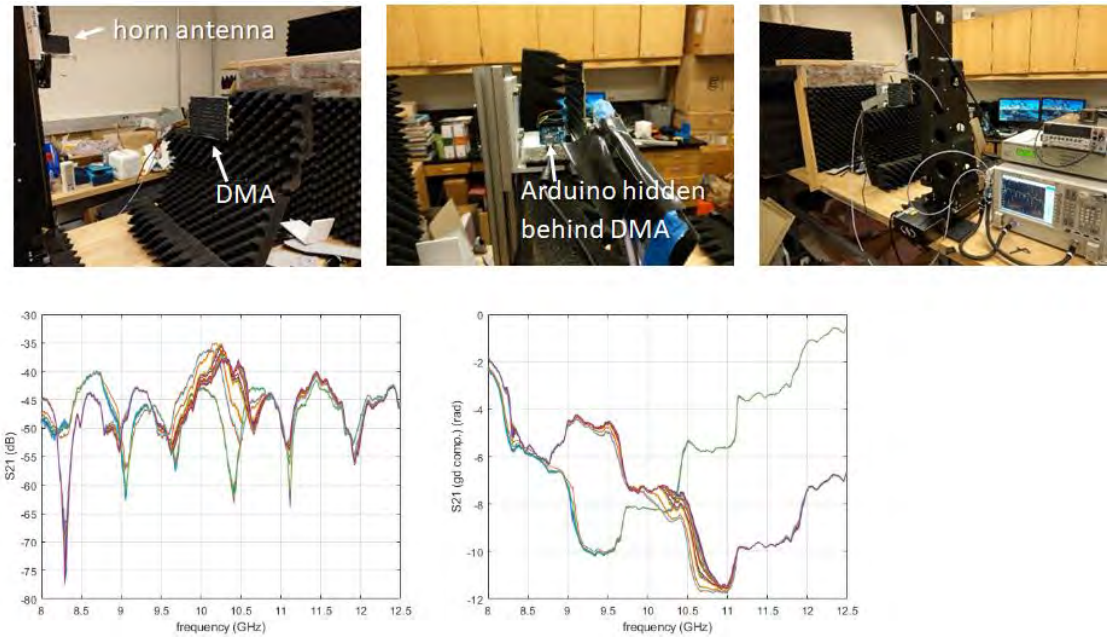

Figure 17 | DMA near-field scan setup and boresight measurement results showing element-to-horn magnitude response for a single horn antenna position and various DMA states of a single DMA element.

DMA Frequency Response

Initial measurements of the DMA showed that the edge-launch feed structure was radiating and, thus, superimposed with the measurements of the DMA element. Fig. 18 shows a comparison of the magnitude and impulse response measurements when the feed structure is covered by absorber (see Fig. 19) and without. It can be clearly seen how the absorber mitigates radiation from the feed structures and measurement of the DMA element itself is greatly improved. For example, the impulse response measurement shows that the unwanted contribution of the feed structures is attenuated by at least 5 dB. This is critical as range gating in the time domain is challenging as the DMA contribution and the contributions of the feed structures are within only three taps (three time bins) which makes windowing approaches impractical.

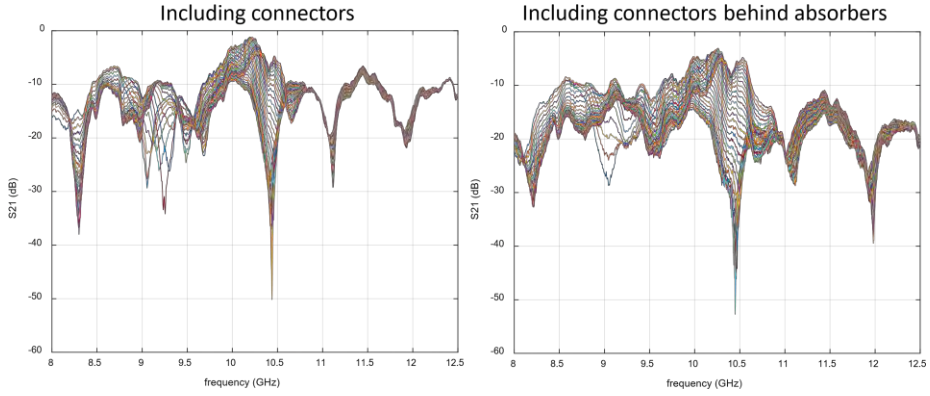

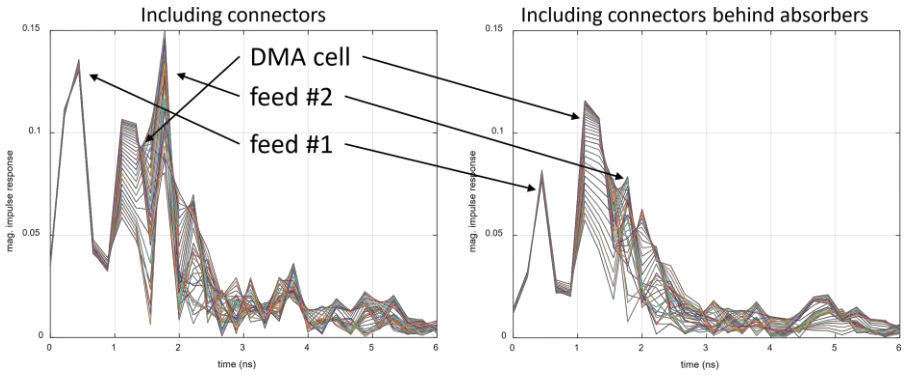

Figure 18 | Comparison of the magnitude and impulse response of a single DMA element without (left) and with (right) shielding of the feed connectors with absorbers.

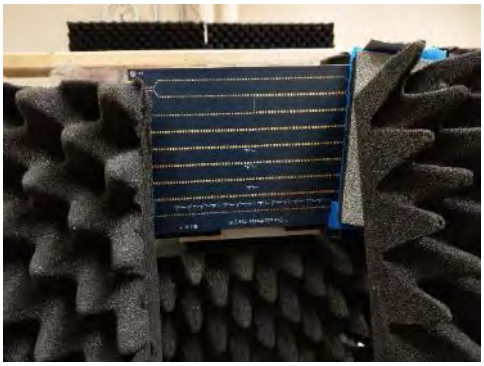

Figure 19 | DMA with feed structures covered with absorbers.

In Fig. 20 the magnitude response of a 2D near field scan for two different frequencies and DMA tuning states is depicted. Although absorbers were used to minimize the influence of the feed structures, the feed structures still influenced the measurements, as evidenced by the deep fading points along the y axis. This is an undesired feature of this particular DMA sample that can be addressed in future designs.

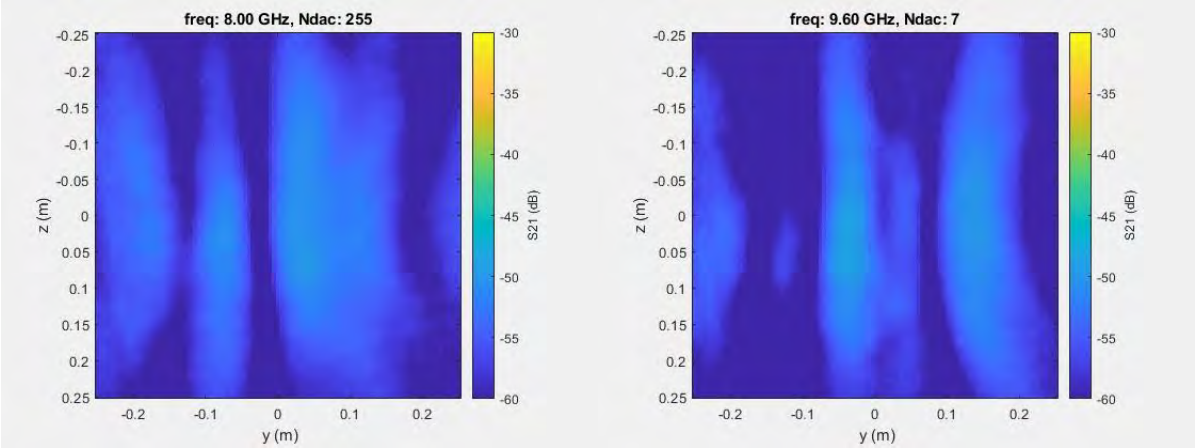

Figure 20 | 2D magnitude response for two different DMA tuning states vs. frequency.

Horn to horn 2D near field scan (NFS) measurements were used to obtain probe calibration data over the full 2D NFS range. Although the used horn antenna is a directive antenna, good NFS results of an appropriately shieled DMA are expected as the horn behaved as expected (see Fig. 21).

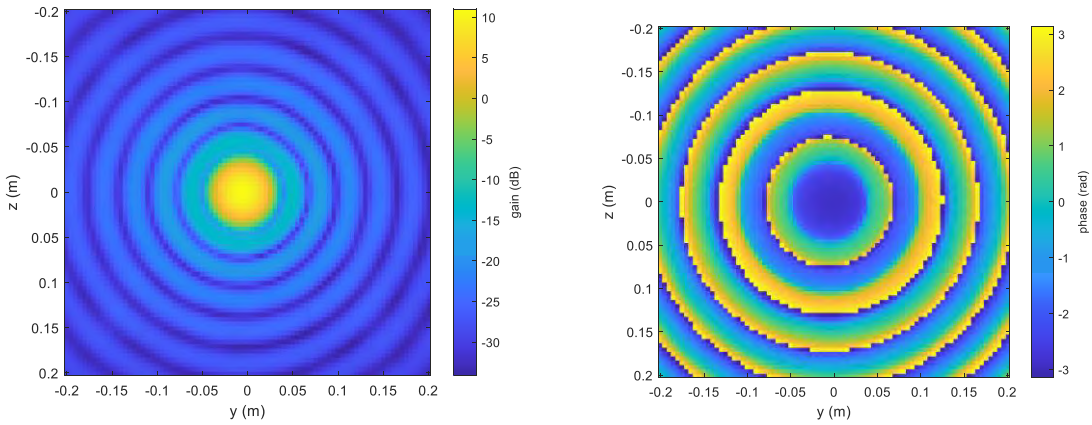

Figure 21 | Back-Projection of the 2D near-field scanned calibration horn measurement. (Left) magnitude response, (right) phase response.

Back-projection of the DMA NFS is shown in Fig. 22**Figure 22** | 2D near-field scanned back-projections of the single DMA case.

. Again, the deep fading due to the parasitic radiation of the feed structures is visible in the magnitude, but also in the phase. An additional NFS with reduced boresight distance between the horn and the DMA was planned to improve 2D resolution, but due to laboratory access

restrictions during to the COVID-19 pandemic this measurement could not be performed (the University of Washington remained in Phase I and II with limited lab access for the duration of this program).

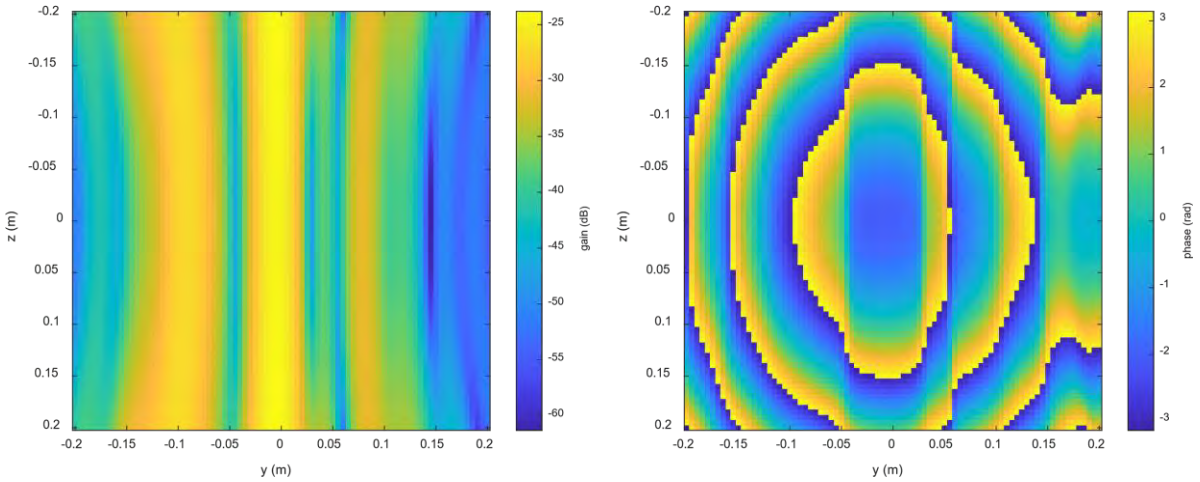

Figure 22 | 2D near-field scanned back-projections of the single DMA case.

Multi-Source System Model for Mitigating Unwanted Feed Radiation

An alternative way to mitigate the feed structure from the measurement in post-processing was explored. The proposed idea was that if the physical distance between the DMA element and the feed structures are geometrically constant and their radiation contribution can be mathematically modeled (see Fig. 23), their emission contribution can be estimated if sufficient measurements can be taken. The received signal is taken as

$$R(j\omega) = [a_0(j\omega)e^{-j\omega\tau_0} + \big(1 - a_0(j\omega)\big)a_1(j\omega, k)\, e^{-j\omega\tau_1} + \big(1 - a_0(j\omega)\big)\big(1 - a_1(j\omega, k)\big)a_2(j\omega)e^{-j\omega\tau_2}]T(j\omega),$$

where $a_0(j\omega)$ is the complex gain of the first feed, τ_0 is some delay between the transmitter and the first feed element, e.g. due to cable delays, $a_1(j\omega, k)$ is the complex gain of the DMA element for given tuning state k, τ_1 is some delay at the DMA element due to cable and delay in the waveguide, $a_2(j\omega)$ is the complex gain of the second feed, τ_2 is some delay due to cable and waveguide, and $T(j\omega)$ is the signal generated by the transmitter. What complicated this approach is that the feed radiation is not independent from the DMA cell, as can be seen by the change of the feed emissions in the impulse response plot for various DMA tuning states. Further investigation will need to be done to determine whether this model leads to a solvable inverse problem or if additional constraints need to be added.

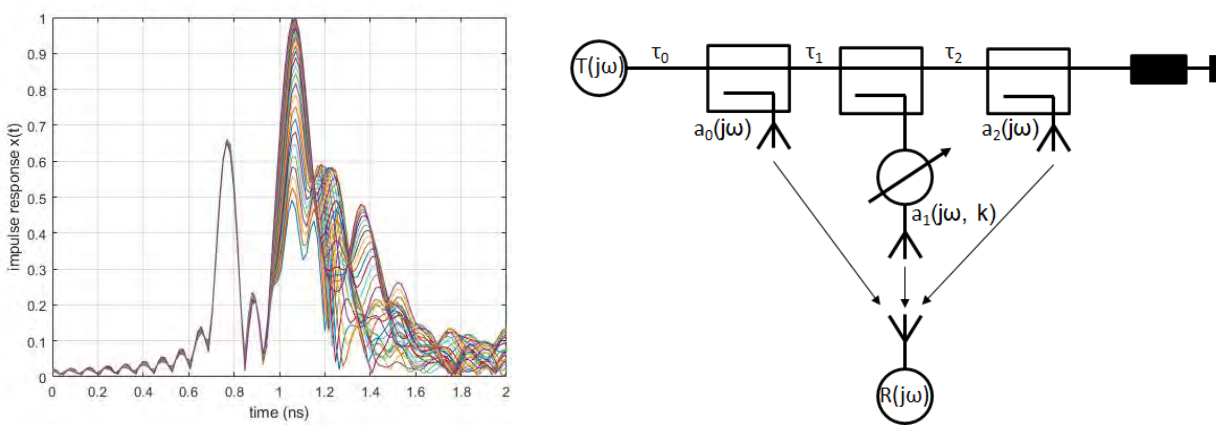

Figure 23 | Impulse response and proposed mathematical model showing the combination of the DMA element and feed structure contribution to the measurement.

Method for estimating Lorentzian parameters for a single DMA cell

Fig. 24 shows the measured Lorentzian magnitude and phase response of a single DMA cell for a boresight measurement for a single frequency (9.6 GHz) but different tuning/code stated (blue). These measurements were used to estimate the parameters of an expanded Lorentzian model given as

$$\varepsilon_{\mathrm{re}} = \frac{\omega_{\mathrm{p}}^2(\omega_0^2 - \omega^2)}{(\omega_0^2 - \omega^2)^2 + \omega^2\gamma^2}$$

$$\varepsilon_{\mathrm{im}} = \frac{\omega_{\mathrm{p}}^2\gamma\omega}{(\omega_0^2 - \omega^2)^2 + \omega^2\gamma^2}$$

$$\varepsilon = (A_0 + A_1\omega) \cdot e^{j(\varphi_0 + \varphi_1\omega)} \cdot (\varepsilon_{re} + j\varepsilon_{im})$$

To estimate the parameters of this model, a nonlinear-least-squares approach was chosen. For this problem the resulting parameters are given as

$$\omega_p = 0.2921$$

$$\omega_0 = 12.25$$

$$\gamma = 6.253$$

$$A_0 = 2.188$$

$$\varphi_0 = 2.574$$

$$A_1 = 0.2566$$

$$\varphi_1 = 0.8425E\text{-}3$$

The normalized mean squared error of this estimation is -24.37 dB, which can be considered to be a good estimation.

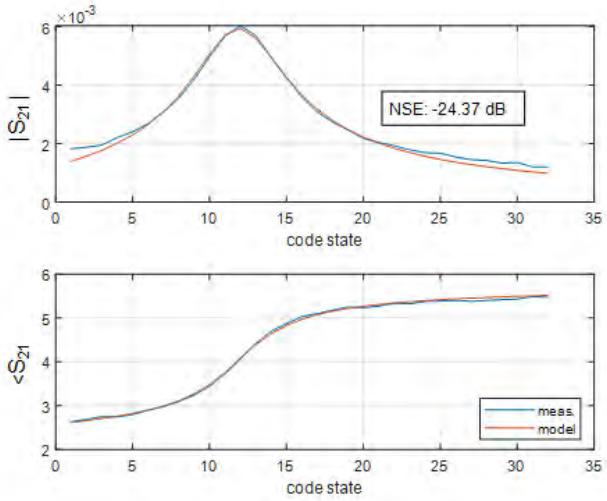

Figure 24 | Lorentzian magnitude and phase response of a DMA element for various tuning/code states.

Method for estimating Lorentzian parameters for multiple DMA cells in parallel

Simulation experiments were used to analyze the performance of estimating the Lorentzian parameters when obtaining measurements of two independent DMA elements simultaneously (see Fig. 25). The simulation assumed, without loss of generality, the linear combination of two elements with random Lorentzian parameters. The number of DMA element tuning states was set to 32 to correspond with the selected sub-range of actual DAC drive currents. Simulations of 100 random tuning states for the array were performed to estimate the Lorentzian parameters and evaluate the normalized mean squared error. 50,000 Monte Carlo runs were performed to obtain reasonable estimation performance statistics.

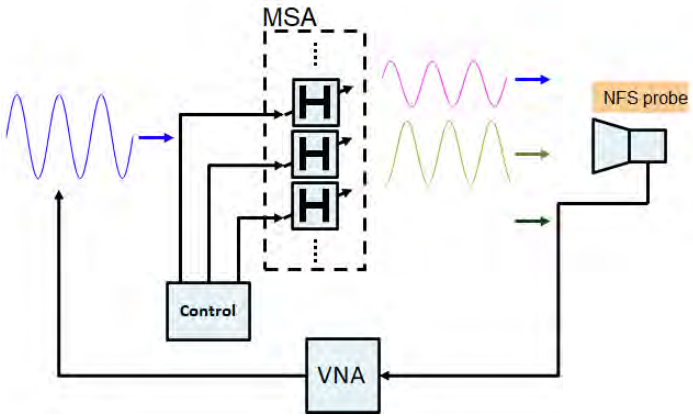

Figure 25 | Measurement of multiple DMA elements in parallel.

Monte Carlo Model: Random codes for controlling many DMA cells

As a first step toward understanding the likely performance of the OCNF approach with many simultaneous DMA cells active, a series of Monte Carlo simulations with fixed "DMA cell" candidates but varying code matrices per iteration were analyzed. The wide spread in the histogram shown in Fig. 26 suggests that the parameter estimation is sensitive to the code matrix. This obviously raises the question of whether there is an "optimum code matrix" (i.e. which combination of tuning states give the best estimation performance). Fig. 27 shows the best estimated parameters for 50,000 Monte Carlo runs. The NSE_{meas} is the normalized mean squared error comparing the "simulated" measurements with the theoretical measurement results given the estimated model parameters. NSE_{model} compares the Lorentzian response of the simulated DMA elements with the Lorentzian response of the estimated model parameters. The measurement error is around -51.0 dB, which we considered to be extremely good. However, the model error is about 10 dB worse at around -43.6 dB, but still excellent. These results suggest that the coded measurement approach will likely be able to disambiguate the contributions of multiple DMA control states in the NF measurement.

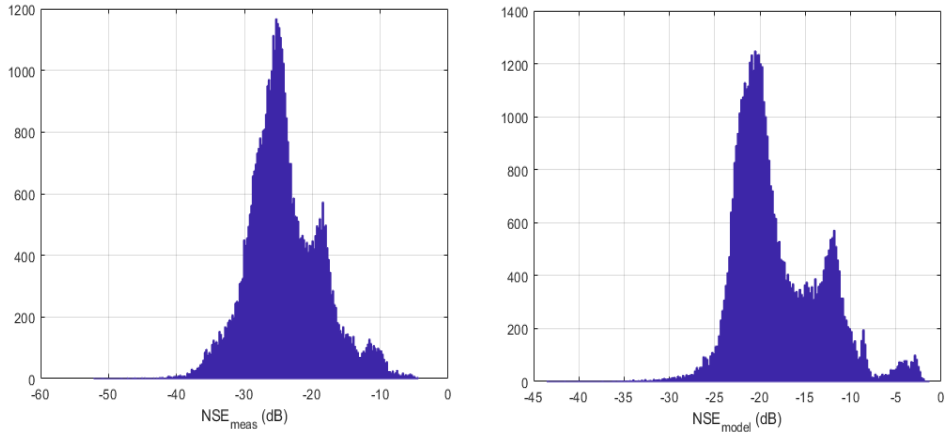

Figure 25 | NSE distribution for the estimation error NSE_{meas} and modeling error NSE_{model}.

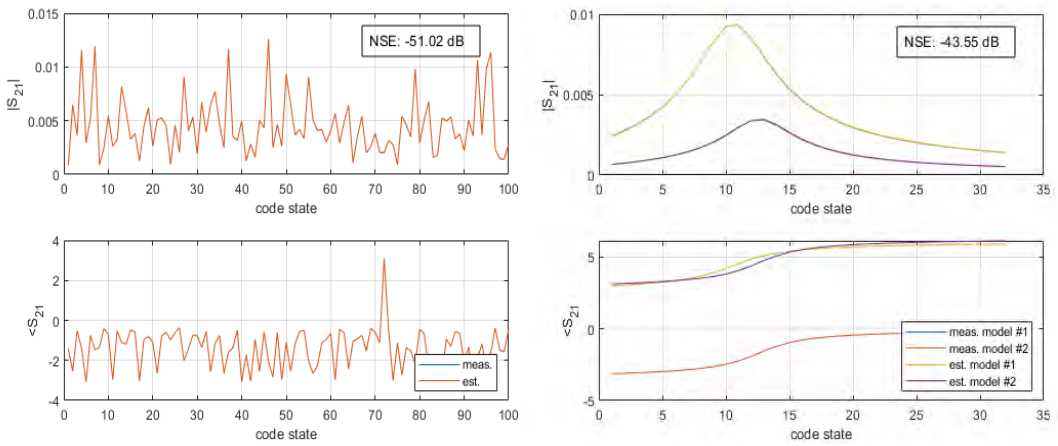

Figure 26 | Best solution of the 50,000 Monte Carlo runs. (left) shows the estimation error, (right) model error.

Monte Carlo: randomized Lorentzian parameters

Here, Monte Carlo simulations with fixed code matrices (see Fig. 27) but random DMA element candidates per iteration were performed. The plot axes correspond to each of the 32 tuning states used for each DMA element.

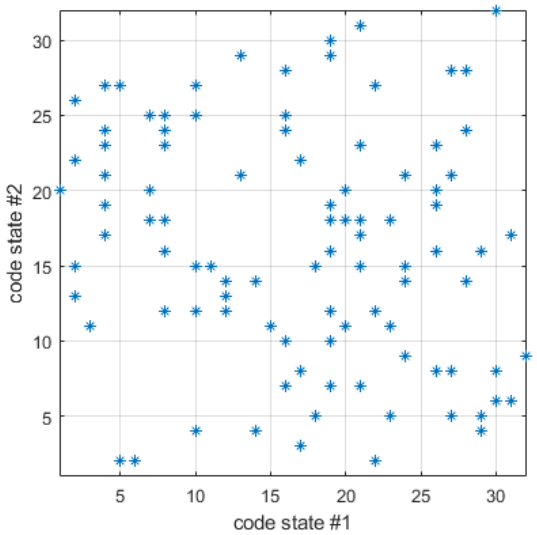

Figure 1: Tuning/Code state matrix.

Figure 27 | Tuning/Code state matrix.

Fig. 28 shows the NSE_{meas} and NSE_{model} distribution for 50,000 Monte Carlo runs. The wide spread in the histogram suggest that the estimation is also sensitive to the DMA element parameters,

but less so than for the code matrix (compare the width of the main peaks). In **Error! Reference source not found.** the best solution of the 50,000 Monte Carlo runs is depicted. The best solution has an NSE_{meas} of -63.74 dB and the NSE_{model} is -45.12 dB. Both values are improved compared to the previously described result, suggesting that an optimum configuration was found.

Generally, this simulation experiment shows that it is feasible to estimate the Lorentzian parameters for independent DMA cells using a combination of various tuning/code states with good performance.

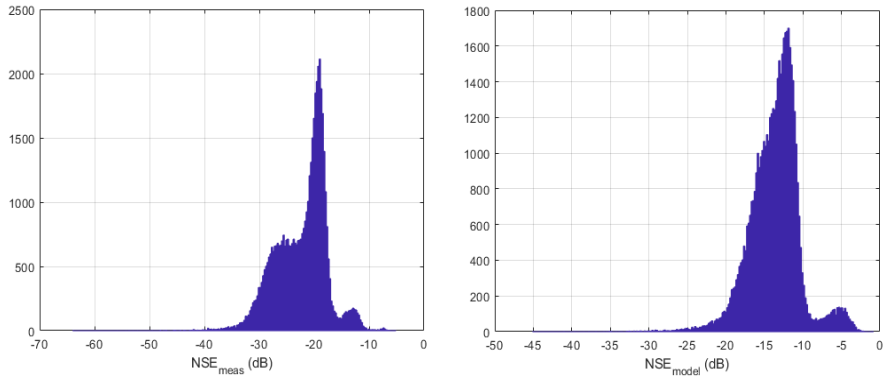

Figure 28 | NSE distribution for the estimation error NSE_{meas} and modeling error NSE_{model}.

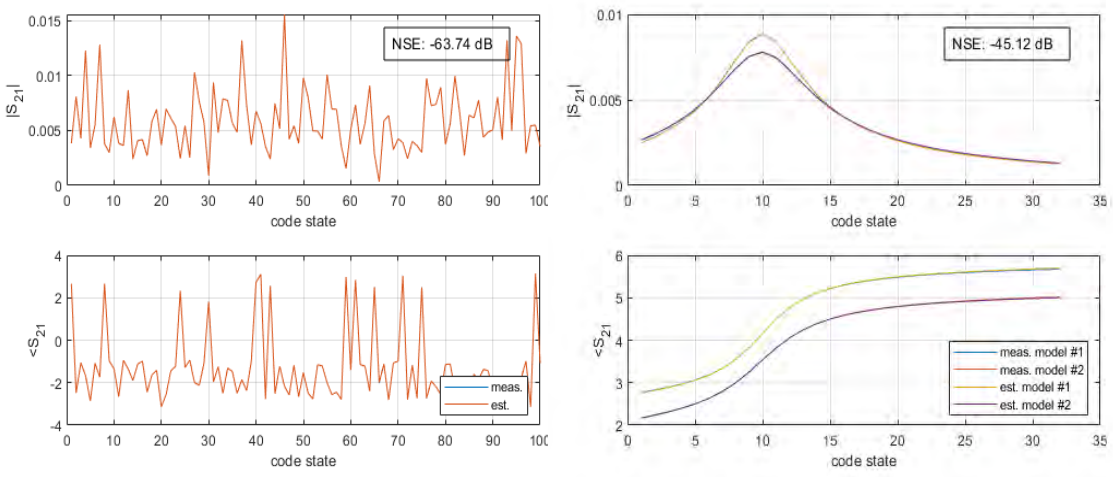

Figure 29 | Best solution of the 50,000 Monte Carlo runs. (left) shows the estimation error, (right) model error.

Conclusion and Future Work

We believe that these results can be leveraged to perform coded measurements of larger DMA samples when larger DMA samples are available. Based on the measurement-based synthetic data set described in this report, we have demonstrated the key premise of the OCNF approach—that the contributions of multiple DMA unit cells can be simultaneously measured via a coded

measurement where NF measurements consisting of multiple DMA control states are successfully disambiguated and translated into parameter models for each DMA unit cell. The codes employed can be either randomized, or optimized for certain classes of DMA unit cell control behavior. In the optimized case, an improvement in DMA unit cell estimation performance (improved ability to disambiguate the contributions of multiple DMA unit cells) has been demonstrated.

THRUST (IV): PROOF-OF-CONCEPT DEMONSTRATION

Work on the experimental proof-of-concept demonstrations went forward at Duke on passive (non-reconfigurable) samples. Initially, a simple 1D structure was fabricated to test out the bending approach we developed during the first reporting period. In a first experiment, we made use of numerical simulations to design a conformal slot antenna, which was subsequently fabricated and tested. In a second, more sophisticated experiment, a metasurface array was designed using the approaches described in Thrust II, also subsequently fabricated and tested. Both of these experiments reveal the capabilities of a metasurface to serve as novel conformal array antennas.

1D sample

With the simulation problems described in the first annual report resolved and having identified an appropriate substrate material showing promising bending capabilities, the final design was modeled in CST Microwave Studio using the frequency domain solver. To reduce simulation time, non-contributing conducting structures are modeled as 2D sheets where possible. The simulation models consist of a two-layer printed circuit board (PCB) base, copper clad with a 20 mil (0.508 mm) Rogers 3003 substrate (ε = 3 between 8-40 GHz and tan δ around 0.010 at 20 GHz). Both a curved and planar version were modeled. While the copper layers act as the top and bottom of the waveguide, the walls are also modeled as layers of copper for convenience. In manufacturing, these walls consist of a layer of thick conductive silver paint, which serve to confine the fields and acts as an excellent conductor.

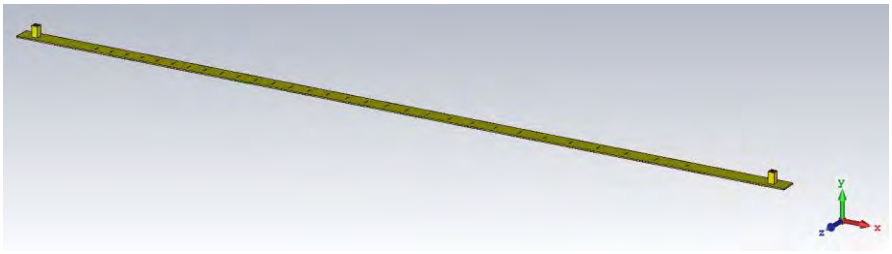

Figure 30 | The planar construction simulated in CST, complete with transitions and connectors.

As discussed in the previous annual report, due to errors produced in the meshing procedure by the simulation software, the planar model, as depicted in Fig. 30, and the curved model in Fig.

31, are built independently, i.e. the curved model was not generated in simulation from the planar model and was instead built from the start to be a curved structure, using basic geometry to translate the apertures and board layers to the appropriate curved orientation. The meshing and convergence of curved structures seem to be an inherent limitation when modeling in CAD full-wave simulators. Smooth surfaces must be discretized to finite polygons, whose density must be fine enough for a smooth approximation but coarse enough such that the simulation time is not unwieldy and the convergence reaches reasonable levels. Choosing the discretization of the polygon in which CST models curved structures to be fine enough for a true, curved representation and yet coarse enough for reasonable simulation time ensures accurate simulation results. Both the planar and curved cases were simulated with and without feed transitions and connectors to confirm agreement between the models.

Figure 30 | The curved model as simulated, again with transitions and connectors.

To confirm simulation and theory results via experimentation, this 28 iris antenna design was manufactured using a copper-clad 20 mil (0.508 mm) Rogers 3003 substrate. The irises were produced using an in-house LPKF S63 milling machine. The antenna was manufactured, shown in Fig. 31, as planar and then attached to a 3D printed fixture to obtain the curved geometry, as shown in Fig. 32. Scattering parameters were obtained from both the planar and curved orientations. The mold itself was designed in CST, fabricated with Ultimaker 2+ model 3D printer, then attached to optical construction rail for ease of hanging the curved structure during characterization. The sample was characterized in a NSI Near Field system, which measures the electric field in the near field. Via FFT, the near field can be propagated to the far field for experimental directivity comparison with simulation.

Figure 31 | The fabricated antenna in the planar case. Silver paint, which comprises the walls of this SIW, is seen in grey along the edges of the guide. The Fairview Microwave SC3030 SMA connector is visible on

the left as is the attachment strip. An annular ring matching structure is patterned on the underside of the connector.

Figure 32 | The same antenna as in Fig. 31 but curved over the mold structure, which can be seen in yellow.

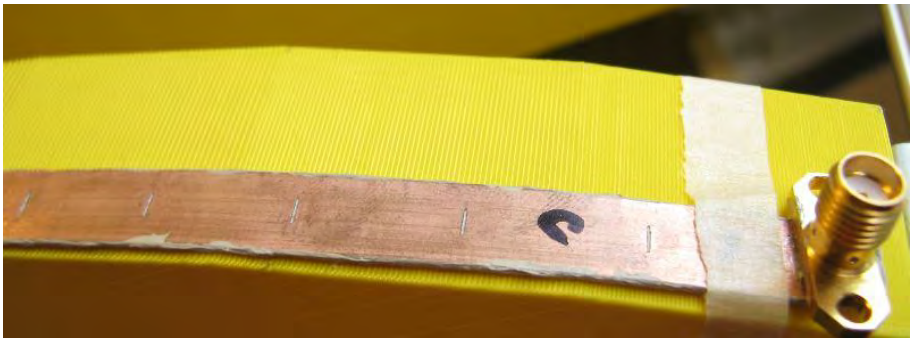

Figure 33 | A closeup of the curved board in Fig. 32.

The scattering parameters were compared between simulation and experiment. As can be seen in Figs. 34 and 35, there is reasonable agreement between the curved and planar simulations of the LWA.

In the S11 parameter, the resonances in the cavity structure of the SIW can be seen, damped by the losses in the SIW. Small perturbations in the experimental signal are assumed to be resonances between couplers. S11 is further raised due to the low power radiated from small, non-resonant irises. Power radiated and efficiency, however, were not design considerations here and could be easily optimized in future design efforts. Also shown are the high losses as frequency increases, further lowering the efficiency of this particular design. S11 at 20 GHz is at -6.48 dB.

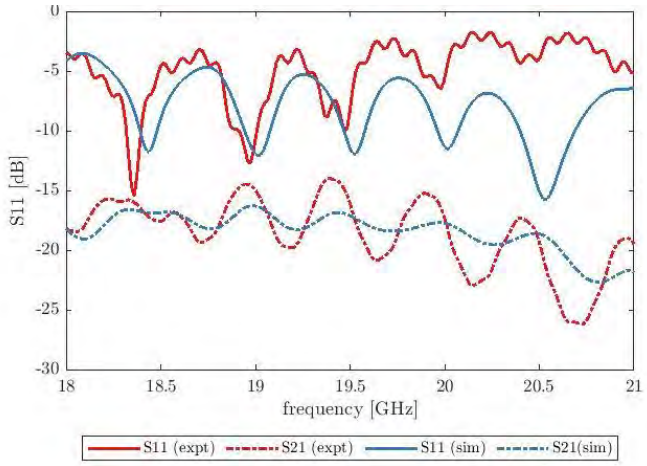

Figure 34 | Shown in this figure are the S-parameters of the planar configuration, comparing simulation and experiment.

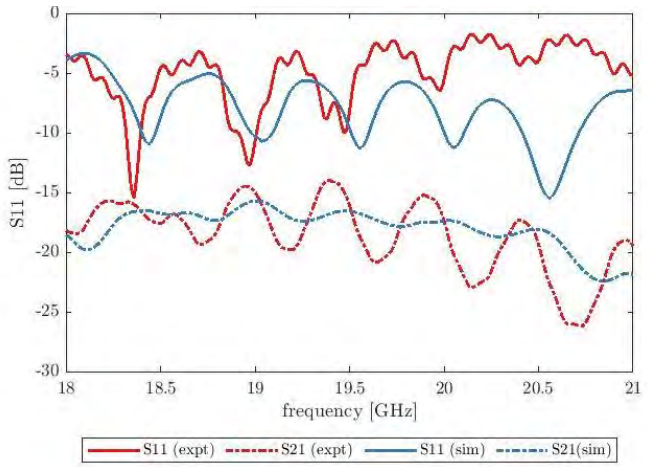

Figure 35 | The S-parameters of the curved structure, also comparing simulation and experiment.

The S21 as measured shows higher loss than as simulated, which is often the case for the fabricated antennas. The higher loss tangent results in a signal that drifts lower as the frequency increases, as expected. The measured S21 at 20 GHz is -17.4 dB.

The design goal for this structure was to produce a directed beam with the bent structure, while also showing that this delicately designed behavior is completely disrupted when the structure is straightened. The initial design of the antenna, as presented in the previous annual report, made use of the following procedure:

Small, identical radiating irises are patterned into the top wall of the waveguide. Each iris, in a first approximation, acts as a polarizable magnetic dipole element. Disregarding interactions

between the elements, which are negligible for small, relatively distant irises used here, we apply a simple holographic approach.

1. A desired output wave and antenna curvature are chosen.
2. From the phase profile of the desired output wave, we determine at which positions along the waveguide the feed wave has the same phase.
3. At such locations, we place identical small irises, each one polarized according to the local phase of the incident feed wave.

Collectively, these induced dipole moments emit radiation into free space that closely corresponds to the desired output wave.

In the experiment, the antenna was curved over a radius of 256.8 mm. As designed, a distinct broadside beam emerges and is readily seen in Fig. 36. The beam shape is clear with good agreement between theory and simulation considering fabrication tolerances and simulation accuracy at such small levels. Side lobe levels in simulation and experiment are below -8.9 dB - 65^{o} and 65^{o} to either side of the main lobe.

In the planar case, the designed behavior vanished, as expected. The general trends of the directivity match between simulation, theory, and experiment. The efficiency of the antenna is very low so the disagreements are likely due to the accuracy limits in the simulation and the achievable fabrication accuracy with the equipment and post processing steps in experiment. Fig. 19 does show an undesirable and indistinct pattern.

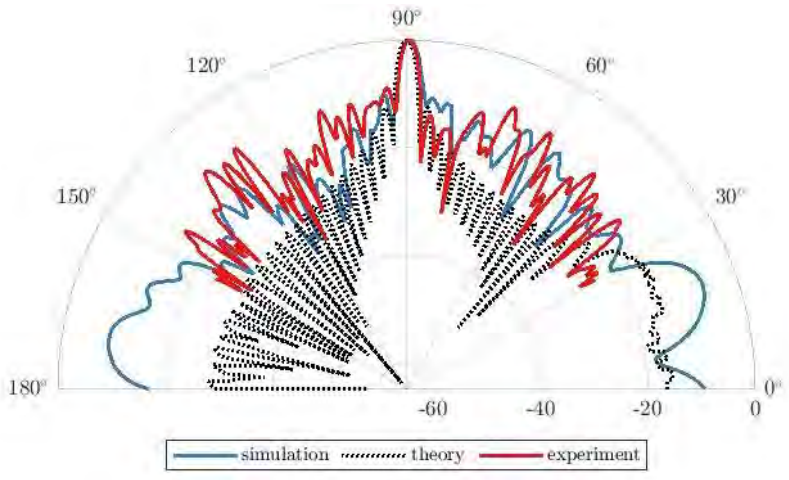

Figure 36 | Comparison of the theoretical, simulated and experimentally measured directivity of the curved antenna, showing a collimated beam as designed for the bent antenna.

The holographic design performed well, producing a beam at 90^{o} when in the curved orientation and producing no pattern in the planar orientation. While the efficiency of the antenna is sub-

optimal, radiated power can be addressed as an additional design parameter now that the holographic method has been demonstrated.

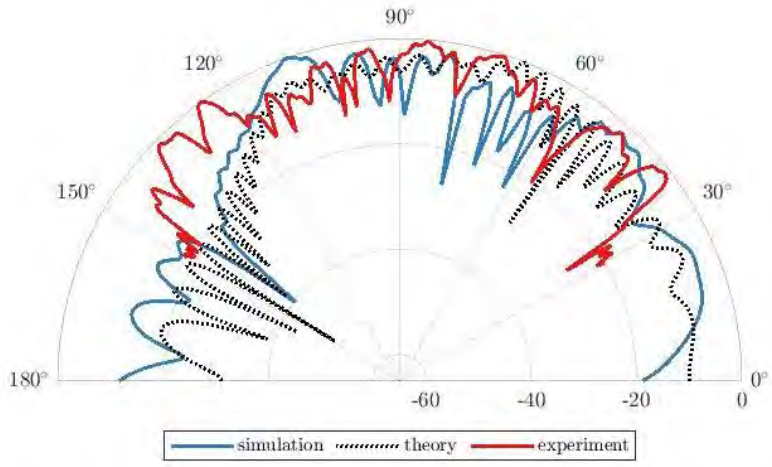

Figure 37 | Comparison of the theoretical, simulated and experimentally measured directivity of the curved antenna, showing a collimated beam as designed for the same antenna as in Fig. 36, but now flattened out and made planar.

Disagreement between theory and simulation is attributed to the accuracy of the CST solver at very small dB levels and to the fabrication limitations of the milling system used. Though the fabrication tolerances are well within the published capability of the system, the heat produced while milling minute, high-eccentricity irises necessitated a good deal of post-processing work, such as removing melted debris from the iris well and deburring the iris edge, which can be seen to have distorted some irises in depth, length and/or eccentricity in Figs. 38 and 39. The mill depth, though calibrated, also likely contributed to shallow over-etching. Taking these slight changes into simulation, applying them to all irises en mass, produced no noticeable difference in simulation, however, simulations were not conducted to incorporate these small changes on an iris-by-iris basis; i.e., due to the simulation time required, no study was completed where Iris 1 was set to have slight over etching and edge irregularity, while Iris 2 had edge irregularity and increased eccentricity, etc. At such low dB, the antenna is susceptible to this accumulation of small irregularities and thus, accounts for the disagreement.

Figure 38 | The as-fabricated antenna, but uncut form the board. The rough edges were processed by hand, clearing out melted substrate and metal filings while deburring the apertures.

Figure 39 | The raw, unprocessed iris on the left compared to the clean iris on the right. Slight irregularity in the iris edge and on the clean sample is readily demonstrated.

Conformal Metasurface Array

The final proof-of-concept experimental demonstration produced by the team consisted of a fabricated and measured conformable metasurface array antenna. Several such passive antennas were produced, designed to illustrate beam steering at different angles. These results illustrate that the design tools work and that conformal metasurface array antennas can be designed and operate as expected.

Using the design approach outlined above based on the CMA-ES optimizer, we designed three conformal metasurface antennas with different beam angles and measured their directivity patterns. Figure 40 shows a photograph of one of the fabricated metasurface antennas before bending. As shown in Fig. 40, the designed metasurface antenna consists of four SIWs each with 15 metamaterial radiators. The metamaterial elements (shown in Fig. 11) with varying gap sizes were etched into the top plate of copper-clad (35 um), 0.762-mm-thick 4003C Rogers substrate. A zoomed-in view of the elements is shown in Fig. 40(c). The SIWs were constructed using vias with a diameter of 0.2 mm. The spacing between adjacent vias was 0.5 mm. The dimensions of the vias were chosen such that the SIW is equivalent to the designed rectangular waveguide illustrated in Fig. 12. In the designed metasurface antennas, the center locations of the metamaterial elements are offset from the middle of each waveguide (i.e., $\pm$0.68 mm). The

spacing between the adjacent metamaterial elements along the waveguide is 5.0 mm (~$0.47\lambda_0$ where λ_0 is the free space wavelength at the operating frequency of 28 GHz). Also, to excite the SIWs, we used the designed four-way power divider connected to an SMA connector, as shown in Fig. 15. Also, we used SIW-to-coaxial transitions depicted in Fig. 15 and connected 50 ohm loads to terminate the SIWs. In the designed antennas, the metasufaces are curved with a radius of curvature equal to 151.2 mm, while the divider and transitions are kept planar. The bending was realized using a 3D printed fixture, as depicted in Figs. 41(a)-(d).

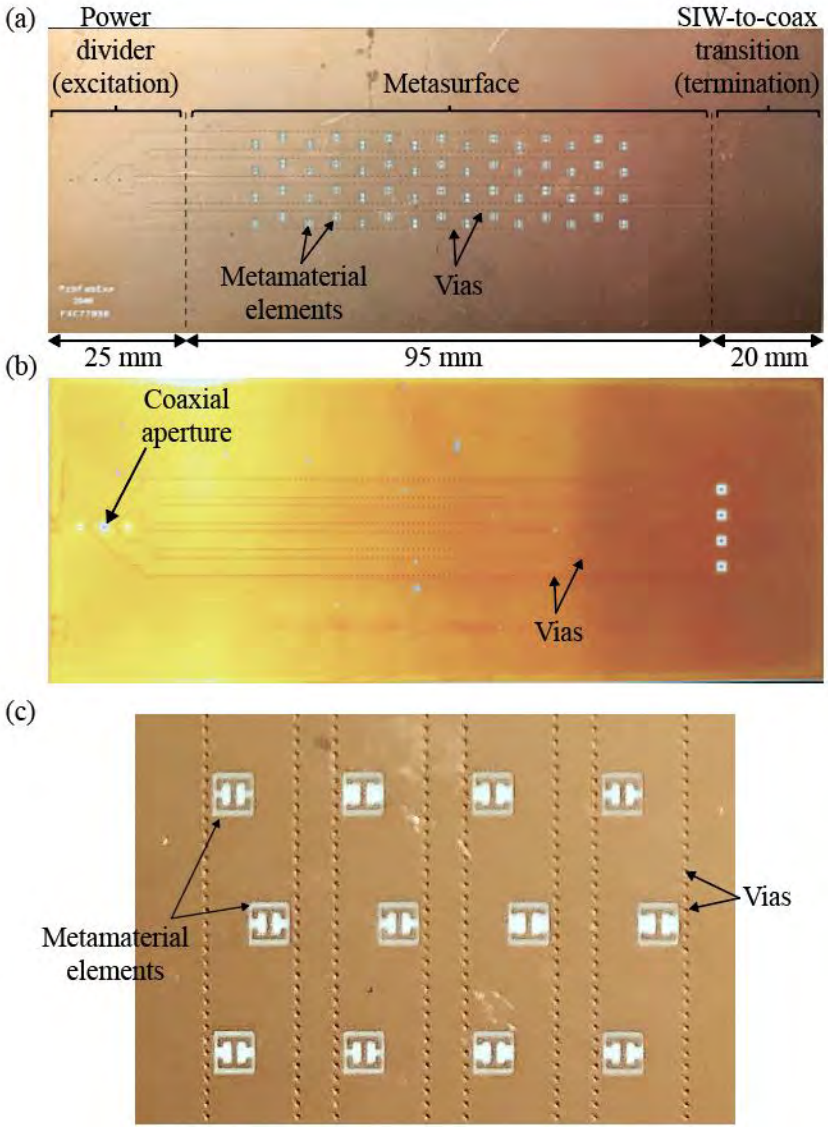

Figure 40 | A photo of the fabricated metasurface antenna generating a beam at ϕ = 70◦ before bending. (a) Top view and (b) bottom view. (c) Zoomed-in view of the metamaterial elements in the metasurface shown in Fig. 40(a).

To obtain the directivity patterns of the fabricated antennas, we used an NSI 2000 scanner and a standard WR-28 probe antenna to measure the near-field scan data and took the fast Fourier

transform (FFT). During the measurement, the fabricated antennas were attached to a 3D printed fixture to ensure the curvature of the metasurfaces. As shown in Fig. 41(a), the middle of the fixture is curved, and the radius of curvature is 151.2 mm while both ends of the fixture are planar to ensure the operation of the power divider and terminators, depicted in Fig. 15. The experimental setup for measurement of the radiation pattern is shown in Fig. 41(e). For comparison, we analyzed the designed metasurface antennas using the full-wave numerical solver and the analytic model of the conformal metasurfaces using the coupled dipole model.

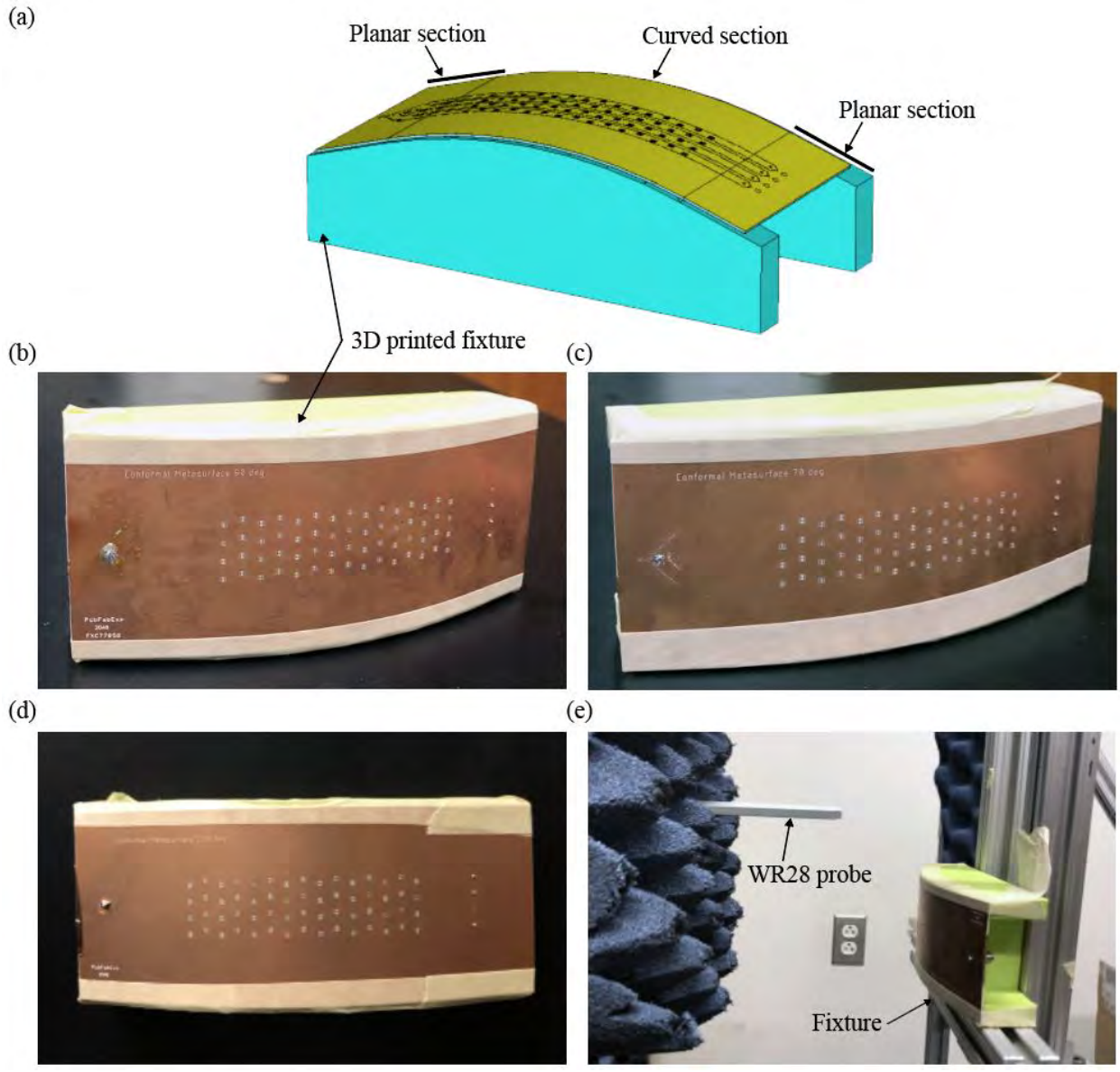

Figure 41 | (a)-(c) A photo of the fabricated metasurface antenna after bending using a 3D printed fixture. During the measurement, each of the fabricated antennas was attached to the 3D printed fixture to ensure the curvature of the metasurfaces in the middle. (d) Experiment setup for measurement of radiation patterns.

Figures 42(a)-(c) show the directivity patterns of the antennas at the target frequency of 28GHz, obtained from the measurements, full-wave analysis, and analytic model. As shown in Figs. 41(a)-(c), the beams are formed at the desired directions, with good agreement between the patterns observed. For the antenna with a beam at (ϕ_{tar},θ_{tar}) = (90◦,90◦), the maximum directivities calculated by the analytic model, full-wave simulation, and measurement are respectively 16.0 dBi, 15.5 dBi, and 17.5 dBi. For the antenna with a beam at (ϕ_{tar},θ_{tar}) = (70◦,90◦), the maximum directivities are respectively 15.7 dBi, 14.8 dBi, and 16.9 dBi. For the antenna with a beam at (ϕ_{tar},θ_{tar}) = (120◦,90◦), the peak directivities are 15.5 dBi, 15.6 dBi, and 16.6 dBi, respectively.

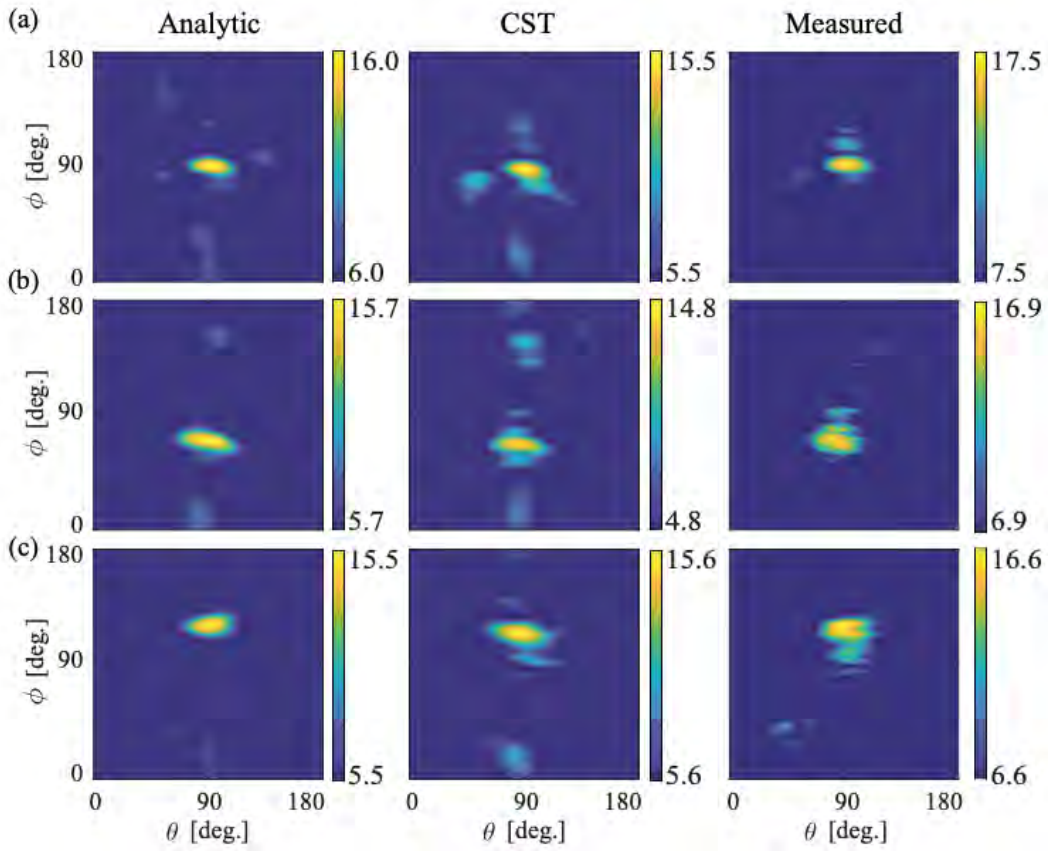

Figure 42 | Directivity patterns of conformal metasurface antenna with a beam at (a) ϕ = 90◦, (b) ϕ = 70◦, and (c) ϕ = 120◦. First column: the analytic method. Second column: full-wave simulations. Third column: measured patterns at 28.0 GHz. The coordinate system defined in Fig. 14 is used.

In Figs. 43(a)-(c), we plot the cross-sections of the radiation patterns in Figs. 42(a)-(c) at the planes of ϕ=90◦ and θ=90◦, respectively. The cross-sectional plots of the patterns also reveal good agreement. For the patterns at θ=90◦, unwanted lobes near the main beam are stronger for the simulated and measured patterns, though the directions at which the main beams appear are as desired. Such mismatches are attributed to certain approximations used in the design method. Also, the patterns at ϕ=90◦ show close agreements.

Note that discrepancies in the patterns are due to the approximations of the analytic model used for the design: First, it is assumed that the curvature of the antenna is small and the field radiated by the metamaterial elements on one side of the bend is not occluded in computing the overall radiation pattern. Second, we have approximated the metamaterial elements as point dipoles, even though they are not in a deeply subwavelength regime. Third, the radiation by the annular rings in the SIW-to-coaxial transitions was not considered in the analytic model. These factors need to be considered to improve the analytical model of conformal metasurface antennas.

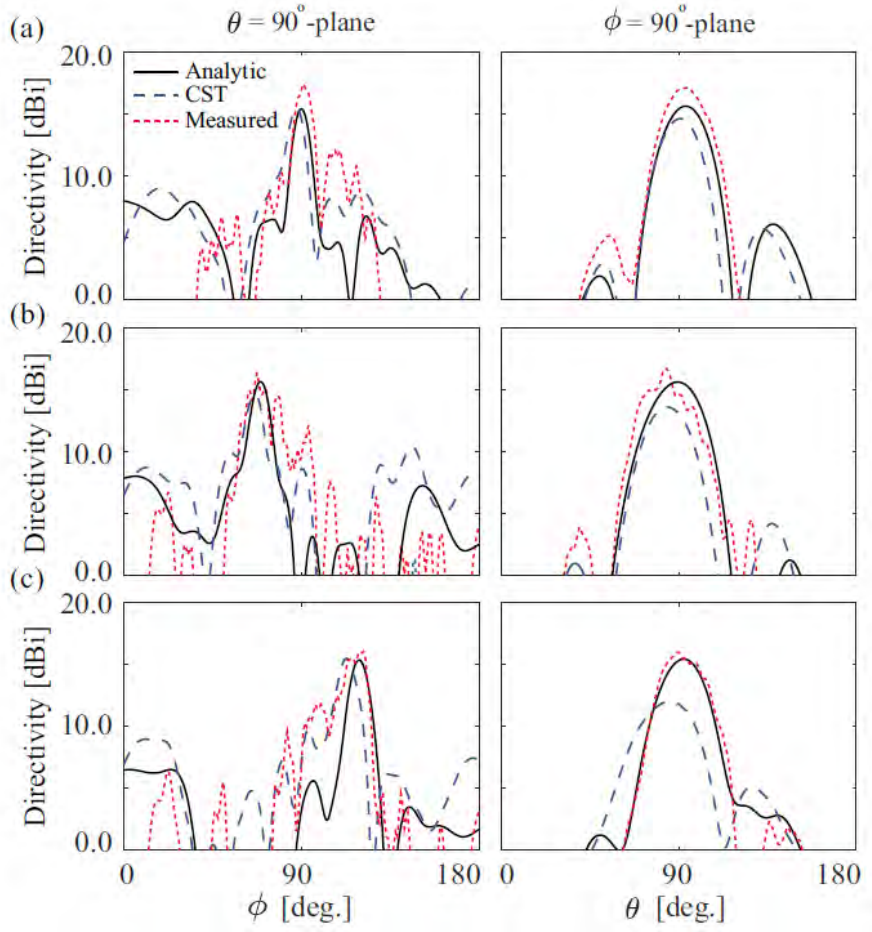

Figure 43 | Cross-sectional plots of directivity of the conformal antennas in Fig. 4. The pattern of the antenna with a beam at (a) ϕ = 90◦, (b) ϕ = 70◦, and (c) ϕ = 120◦.

References

1. IEEE Standard Definition: IEEE Std 145-1993, 2.74.
2. L. Josefsson and P. Persson, *Conformal Array Antenna Theory* (IEEE, 2006).
3. L. Josefsson and P. Persson, "Conformal Array Antennas," in *Handbook of Antenna Technologies* (Springer, 2015).

4. D. R. Smith, O. Yurduseven, L. Pulido-Mancera, P. T. Bowen, "Analysis of a waveguide-fed metasurface antenna," *Phys. Rev. Appl.* **8**, 054048 (2017).
5. J. N. Gollub *et al.*, "Large metasurface aperture for millimeter wave computational imaging at the human-scale," *Scientific Reports* **7**, 42650 (2017).
6. See, for example, Kymeta Corp. (www.kymetacorp.com); Echodyne Corp. (www.echodyne.com); and Pivotal Commware (https://pivotalcommware.com).
7. N. Kundtz, D. R. Smith, J. B. Pendry, "Electromagnetic design with transformation optics," *Proceedings of the IEEE* **99**, 1622 (2010).